SUBMITTED MANUSCRIPT

Published version available at: https://www.sciencedirect.com/science/article/pii/S0307904X21002845
DOI: https://doi.org/10.1016/j.apm.2021.05.024

Equivalent-Single-Layer discontinuous Galerkin methods for multilayered shells

Giuliano Guarino[a], Alberto Milazzo[a], Vincenzo Gulizzi[b,*]

[a] *Department of Engineering, University of Palermo, Viale delle Scienze, Edificio 8, Palermo, 90128, Italy*
[b] *Center for Computational Sciences and Engineering (CCSE), Lawrence Berkeley National Laboratory MS, 50A-3111, 1 Cyclotron Rd, Berkeley, 94720, CA, United States*

Abstract

An original formulation for the elastic analysis of multilayered shells is presented in this work. The key features of the formulation are: the representation of the shell mean surface via a generic system of curvilinear coordinates; the unified treatment of general shell theories via an Equivalent-Single-Layer approach based on the through-the-thickness expansion of the covariant components of the displacement field; and an Interior Penalty discontinuous Galerkin scheme for the solution of the set of governing equations. The combined use of these features enables a high-order solution of the multilayered shell problem. Several numerical tests are presented for isotropic, orthotropic and multilayered shells with different geometrical configurations and boundary conditions, including the case of a non-smooth geometry. Comparisons with analytical solutions and finite-element simulations show the high-order accuracy as well as the capability and robustness of the proposed formulation, which can be a valuable tool for the analysis of generally-curved multilayered shells.

Keywords: Multilayered shells, Equivalent-Single-Layer theories, Discontinuous Galerkin Methods, High-order modelling

1. Introduction

Composite multilayered shells are employed in aerospace, automotive and civil engineering as weight-saving structural components and are increasingly becoming the preferred choice over their metallic counterparts thanks to the possibility of fine-tuning the stacking sequence and the orientation of the constituent layers [1, 2]. As opposed to plates, shells are characterized by a non-flat mean surface and display the *curvature effect*, i.e. an effect of structural stiffening due to the geometric curvature [3]. However, despite its versatility, the interplay between the curved geometry and the properties of the composite layers induces a complex distribution of the mechanical fields, such strains and stresses, which must be accurately resolved to safely employ generally-curved composite shells as load-bearing structures. In fact, the study of the mechanical response of laminated shells is currently an active area of research, see e.g. [4, 5, 6, 7].

In general, the analysis of composite multilayered shells is a three-dimensional (3D) problem that requires the use of computational methods as analytical solutions are limited to very few special cases as shown, for instance, in [8, 9, 10, 11]. Fully 3D models are very accurate but might be overly demanding in computational resources and ineffective at the early design stage. On the

*Corresponding author.
Email addresses: giuliano.guarino@unipa.it (Giuliano Guarino), alberto.milazzo@unipa.it (Alberto Milazzo), vgulizzi@lbl.gov (Vincenzo Gulizzi)

other hand, the problem can be addressed through the so-called two-dimensional (2D) theories, which are based on suitable assumptions on the behavior of the mechanical fields throughout the thickness of the considered structures and are a viable strategy for reducing the computational complexity with respect to 3D models.

The most emblematic examples of 2D theories are the Classical Laminated Theory (CLT) [12, 13] and the First-order Shear Deformation Theory (FSDT) [14, 2], which are based on a linear through-the-thickness approximation of the in-plane displacements but differ in the treatment of components of the out-of-plane shear strains. Typically, the CLT performs well for thin, isotropic plates or shells, whereas the FSDT is recommended when moderately thicker, laminated structures are considered [2]. Motivated by the need for more accurate models, researchers have therefore enriched the through-the-thickness assumptions and introduced the so-called *higher-order* theories for plate and shells, which can be classified into: Equivalent-Single-Layer (ESL) theories [15, 16, 17, 18, 19], whereby the layers are replaced by a single layer with equivalent mechanical properties, Layer-Wise (LW) theories [20, 21, 22, 23, 24, 25], whereby each layer is treated independently, and sub-laminate theories [26], whereby groups of layers are replaced by groups of equivalent layers. A unified descriptions of these approaches has been introduced by the Carrera Unified Formulation (CUF) [27, 28, 29], which provides a framework able to determine the best 2D theory in terms of computational efficiency versus solution accuracy for a given structural problem [6]. Further approaches to the modelling of shell-like structures include the continuum-based solid-shell models [30], which are based on displacement degrees of freedom only, and the variable-kinematics models [31, 32], where different structural theories are employed for different regions of the same structure.

In most cases, numerical models based on these theories are solved using the Finite Element Method (FEM). Recent formulations include high-order FEM approaches [33, 34], the work by Versino et al.[35, 36, 37] on a four-node finite element for doubly-curved laminated shells modelled via a refined zig-zag theory, the FEM models based on the CUF [38], and the modified FSDT for piezoelectric shells by Mallek et al.[39]. The reader interested in a more comprehensive review on shell theories and the related FEM models is referred to Ref.[40].

Numerical strategies have also been proposed as an alternative to FEM: Wu and Li.[41] employed the Differential Quadrature method for conical shells modelled by the FSDT; Tornabene et al.[42, 19, 24, 43] employed the closely related Generalized Differential Quadrature method for studying doubly-curved shells in the context of both ESL and LW theories; Ferreira et al.[44] proposed the use of a collocation method based on radial basis functions for the study of doubly-curved shells modelled via LW theories; Behrami et al.[45] developed a Spectral Element Method for the vibration analysis of thin shallow shells.

A powerful numerical technique, which was firstly introduced for hyperbolic partial differential equations (PDEs) [46] and subsequently outlined in the the context of elliptic PDEs [47], is the discontinuous Galerkin (dG) method. Similarly to FEM, dG methods rely on a discretization, or mesh, of the analysed domain; however, unlike the majority of numerical schemes, the dG approach is based on a discontinuous representation of the numerical solution over the mesh elements and on the use of suitably defined inter-element boundary integrals to recover the solution continuity and enforce the boundary conditions. Such a feature enables in dG-based formulations the seamless use of high-order elements and hierarchical meshes with tunable *hp*-refinement. As regards its application to the theories of plate and shell structures, the dG method has been adopted for the CLT [48, 49, 50, 51], the FSDT [52, 53, 54] and more recently, for the analysis of elastic [55, 56] and piezoelectric [57] multilayered plates modelled by ESL and LW theories. It is also worth noting that the dG method shares several features with the Nitsche's method [58] and a penalty-based Ritz's approach [59, 60, 61, 7], which have been employed for the analysis of assembly of plate

and shell structures modelled via the FSDT. However, to the best of the Authors' knowledge, a dG-based formulation for multilayered shells modelled via high-order theories is not available in the literature.

In this work, we therefore present a family of Equivalent-Single-Layer discontinuous Galerkin schemes for generally-curved multilayered shells. With respect to the existing literature, the proposed approach offers a high-order description of the variables of interest over the whole shell domain via the combined use of a displacement-based ESL assumption, which allows for different through-the-thickness expansion orders of the displacement components, and an Interior Penalty dG scheme, which allows for a high-order numerical solution of the governing equations throughout the shell modeling domain. Moreover, the formulation is not limited to the use of orthogonal curvilinear coordinates and is able to handle shell structures whose mean surface is described via generic parametrizations.

The paper is organized as follow: Sec.(2) introduces the description of the considered multilayered shells in terms of geometry, constitutive behavior and through-the-thickness ESL assumptions; Sec.(2) also introduces the governing equation of ESL shells and Sec.(3) outlines the Interior Penalty dG scheme employed for their solution; Sec.(4) presents the numerical tests conducted on shells with different geometries, materials and boundary conditions; the obtained results are compared with those computed via analytical solutions and FEM models. Eventually, Sec.(5) summarizes the remarks of this work.

2. Problem statement

This work focuses on the elastic problem for composite multilayered shells. The generic shell consists of N_ℓ composite layers. The ℓ-th layer is characterized by its thickness $\tau^{\langle\ell\rangle}$ and by an angle $\theta^{\langle\ell\rangle}$, which describes the orientation of the fibers as discussed in Sec.(2.3). Each layer is assumed to be homogeneous, linear elastic and perfectly bonded through the inter-layer interfaces.

The shells is referred to a Cartesian reference system spanned by the coordinates $\{x_1, x_2, x_3\}$ and occupies the volume V with boundary $S \equiv \partial V$. Similarly, the volume of the ℓ-th layer is denoted with $V^{\langle\ell\rangle}$ and its boundary with $S^{\langle\ell\rangle} \equiv \partial V^{\langle\ell\rangle}$. In the continuation of the paper, the superscript $\langle\ell\rangle$ will denote a quantity related to the ℓ-th layer, Greek subscripts will take values in $\{1, 2\}$, Latin indices will take values in $\{1, 2, 3\}$ and Einstein's implied summation convention over repeated indices will be employed unless explicitly stated otherwise.

2.1. Geometry description

The description of the geometry of the considered shells is given in terms of an analytic function $\boldsymbol{x}_0 : \Omega_\xi \to \mathbb{R}^3$ that defines its mean surface as $\boldsymbol{x}_0 = \boldsymbol{x}_0(\xi_1, \xi_2)$, where $\{\xi_1, \xi_2\}$ denotes the set of curvilinear coordinates spanning the so-called *reference domain* Ω_ξ of the shell. The expression of the mean surface allows to compute the unit normal vector $\boldsymbol{a}_3$ as

$$\boldsymbol{a}_3(\xi_1, \xi_2) = \frac{\boldsymbol{a}_1 \times \boldsymbol{a}_2}{||\boldsymbol{a}_1 \times \boldsymbol{a}_2||}, \quad \text{with } \boldsymbol{a}_\alpha \equiv \frac{\partial \boldsymbol{x}_0}{\partial \xi_\alpha}, \tag{1}$$

and describe the location of the generic point $\boldsymbol{x} \in V$ according to the following expression

$$\boldsymbol{x}(\xi_1, \xi_2, \xi_3) \equiv \boldsymbol{x}_0(\xi_1, \xi_2) + \xi_3 \boldsymbol{a}_3(\xi_1, \xi_2), \quad \text{for } \{\xi_1, \xi_2, \xi_3\} \in \Omega_\xi \times I_{\xi_3}, \tag{2}$$

where $I_{\xi_3} \equiv [-\tau/2, \tau/2]$ is the interval spanned by the curvilinear variable ξ_3 and $\tau \equiv \sum_{\ell=1}^{N_\ell} \tau^{\langle\ell\rangle}$ denotes the total thickness of the shell.

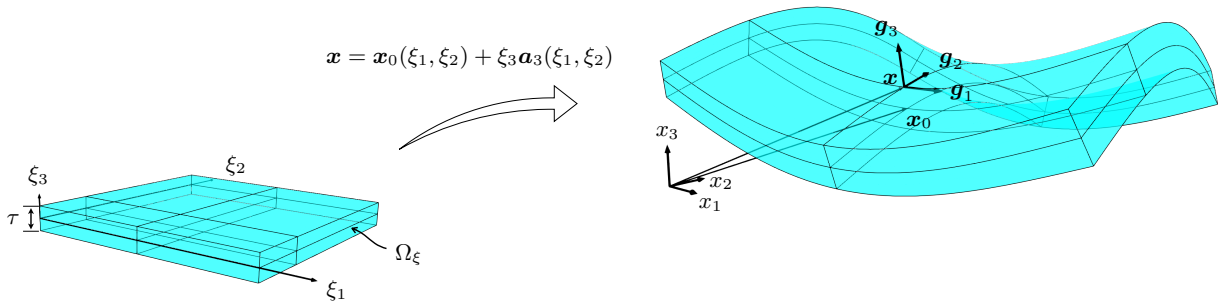

Figure 1: (a) Reference space spanned by the curvilinear coordinates $\{\xi_1, \xi_2, \xi_3\}$. (b) Sample mapped geometry showing the covariant basis at the generic point in the shell volume.

By differentiating the mapping given in Eq.(2) with respect to the curvilinear coordinates, it is possible to introduce: the associated *covariant basis*, whose vectors are $\boldsymbol{g}_1 \equiv \partial \boldsymbol{x}/\partial \xi_1$, $\boldsymbol{g}_2 \equiv \partial \boldsymbol{x}/\partial \xi_2$ and $\boldsymbol{g}_3 \equiv \partial \boldsymbol{x}/\partial \xi_3 \equiv \boldsymbol{a}_3$; the *contravariant basis*, whose vectors $\boldsymbol{g}^i$ are defined by $\boldsymbol{g}^i \cdot \boldsymbol{g}_j = \delta^i_j$, being δ^i_j the Kronecker delta function; and the corresponding covariant and contravariant components of the metric tensor, which are computed as $g_{ij} = \boldsymbol{g}_i \cdot \boldsymbol{g}_j$ and $g^{ij} = \boldsymbol{g}^i \cdot \boldsymbol{g}^j$, respectively. It is worth noting that the use of subscripts and superscripts strictly follows the lower and upper indices notation only to indicate the vectors of the covariant and contravariant bases and the components of the metric tensor; in all other cases, standard subscripts are used. A schematic representation of the reference space spanned by the coordinates $\{\xi_1, \xi_2, \xi_3\}$ is shown in Fig.(1a), whereas a sample mapped geometry and the vectors of the associated covariant basis at a point $\boldsymbol{x} \in V$ are shown in Fig.(1b).

Eventually, given the map (2), the following relations hold [62]

$$\mathrm{d}V = \sqrt{g}\ \mathrm{d}V_\xi \quad \text{and} \quad \mathrm{d}S = \sqrt{g}\sqrt{n_i g^{ij} n_j}\ \mathrm{d}S_\xi \tag{3}$$

where $\mathrm{d}V$ is the Cartesian volume element, $\mathrm{d}S$ is the Cartesian surface element, $\mathrm{d}V_\xi$ is the curvilinear volume element, $\mathrm{d}S_\xi$ is the curvilinear surface element, $g \equiv \det(g_{ij})$ and n_i is the i-th Cartesian components of the outer unit normal at $\boldsymbol{x} \in S$. Moreover, the relationship between the Cartesian components v_i of a generic vector $\boldsymbol{v}$ and its covariant curvilinear components v_{ξ_i} can be written using the following matrix notation

$$\boldsymbol{v} = \boldsymbol{R}\boldsymbol{v}_\xi, \tag{4}$$

where $\boldsymbol{v} \equiv \{v_1, v_2, v_3\}^\intercal$, $\boldsymbol{v}_\xi \equiv \{v_{\xi_1}, v_{\xi_2}, v_{\xi_3}\}^\intercal$ and $\boldsymbol{R}$ is a transformation matrix whose i-th column coincides with $\boldsymbol{g}^i$.

2.2. Strain-displacement relations

Let us introduce the vector $\boldsymbol{u} \equiv \{u_1, u_2, u_3\}^\intercal$, which collects the displacement components in the Cartesian reference system, and the strain vector $\boldsymbol{\gamma} \equiv \{\gamma_{11}, \gamma_{22}, \gamma_{33}, \gamma_{23}, \gamma_{13}, \gamma_{12}\}^\intercal$, which collects the Cartesian components of the small strain tensor according to the Voigt notation. Following Refs.[55, 56], the relation between the strain and the displacement are written using the expression

$$\boldsymbol{\gamma} = \boldsymbol{I}_i \frac{\partial \boldsymbol{u}}{\partial x_i}, \tag{5}$$

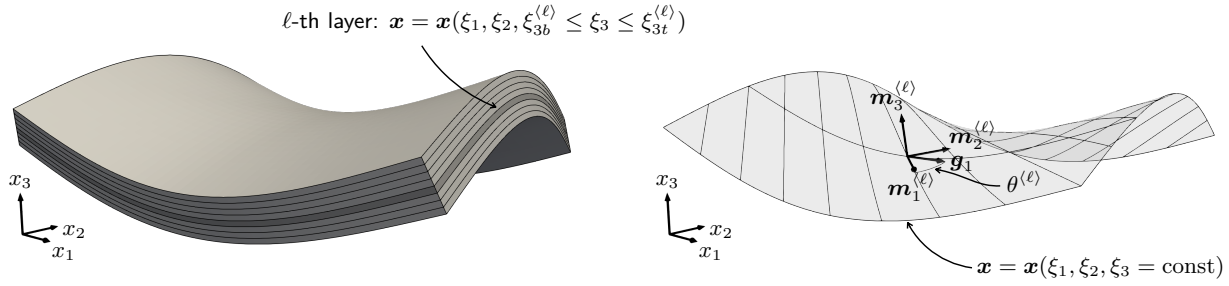

(a) (b)

Figure 2: (a) Schematic representation of a multilayered shell where the generic ℓ-th layer is shown in darker color. (b) Fibers orientation at a slice $\boldsymbol{x} = \boldsymbol{x}(\xi_1, \xi_2, \xi_3 = \text{const})$ of the ℓ-th lamina.

where $\boldsymbol{I}_i$ are 6×3 constant matrices given by

$$\boldsymbol{I}_1 \equiv \begin{bmatrix} 1 & 0 & 0 \\ 0 & 0 & 0 \\ 0 & 0 & 0 \\ 0 & 0 & 0 \\ 0 & 0 & 1 \\ 0 & 1 & 0 \end{bmatrix}, \quad \boldsymbol{I}_2 \equiv \begin{bmatrix} 0 & 0 & 0 \\ 0 & 1 & 0 \\ 0 & 0 & 0 \\ 0 & 0 & 1 \\ 0 & 0 & 0 \\ 1 & 0 & 0 \end{bmatrix} \quad \text{and} \quad \boldsymbol{I}_3 \equiv \begin{bmatrix} 0 & 0 & 0 \\ 0 & 0 & 0 \\ 0 & 0 & 1 \\ 0 & 1 & 0 \\ 1 & 0 & 0 \\ 0 & 0 & 0 \end{bmatrix}. \tag{6}$$

Moreover, upon introducing the vector $\boldsymbol{u}_\xi \equiv \{u_{\xi_1}, u_{\xi_2}, u_{\xi_3}\}^\intercal$ containing the covariant components of the displacement field, and substituting Eq.(4) into Eq.(5), it is possible to express the strain $\boldsymbol{\gamma}$ as a function of $\boldsymbol{u}_\xi$ as follows

$$\boldsymbol{\gamma} = \boldsymbol{I}_i \frac{\partial(\boldsymbol{R}\boldsymbol{u}_\xi)}{\partial \xi_j} \frac{\partial \xi_j}{\partial x_i}. \tag{7}$$

2.3. Constitutive behavior

The constitutive behavior of the considered shell is determined by the constitutive behavior of its layers, which are assumed to be orthotropic laminae stacked in such a way that they follow the curvature of the shell surface as shown in Fig.(2a). More specifically, given the coordinates $\xi_3 = \xi_{3b}^{\langle\ell\rangle}$ and $\xi_3 = \xi_{3t}^{\langle\ell\rangle} = \xi_{3b}^{\langle\ell\rangle} + \tau^{\langle\ell\rangle}$ of the ℓ-th layer's bottom and top reference surfaces, respectively, the volume $V^{\langle\ell\rangle}$ of the layer is assumed to coincide with the points $\boldsymbol{x} = \boldsymbol{x}(\xi_1, \xi_2, \xi_{3b}^{\langle\ell\rangle} \leq \xi_3 \leq \xi_{3t}^{\langle\ell\rangle})$. Then, at each point $\boldsymbol{x}$ of the layer's volume $V^{\langle\ell\rangle}$, it is possible to introduce the material local reference system identified by the unit vectors $\boldsymbol{m}_1^{\langle\ell\rangle}$, $\boldsymbol{m}_2^{\langle\ell\rangle}$ and $\boldsymbol{m}_3^{\langle\ell\rangle}$, which are defined as

$$\boldsymbol{m}_3^{\langle\ell\rangle} \equiv \boldsymbol{a}_3, \quad \boldsymbol{m}_1^{\langle\ell\rangle} \equiv \boldsymbol{R}_{\boldsymbol{a}_3}(\theta^{\langle\ell\rangle}) \frac{\boldsymbol{g}_1}{||\boldsymbol{g}_1||} \quad \text{and} \quad \boldsymbol{m}_2^{\langle\ell\rangle} \equiv \boldsymbol{m}_3^{\langle\ell\rangle} \times \boldsymbol{m}_1^{\langle\ell\rangle}, \tag{8}$$

where $\boldsymbol{R}_{\boldsymbol{a}_3}$ is a matrix that performs a rotation of the angle $\theta^{\langle\ell\rangle}$ around the axis $\boldsymbol{a}_3$, being $\theta^{\langle\ell\rangle}$ the orientation associated to the fibers of ℓ-th lamina. It is worth noting that for general curvilinear coordinates, the vectors $\boldsymbol{m}_1^{\langle\ell\rangle}$, $\boldsymbol{m}_2^{\langle\ell\rangle}$ and $\boldsymbol{m}_3^{\langle\ell\rangle}$ not only are different from layer to layer but they continuously vary within each layer according to the definition given in Eq.(8). As an example, Fig.(2b) shows the material reference system and the angle between the vector $\boldsymbol{g}_1$ and the unit vector $\boldsymbol{m}_1^{\langle\ell\rangle}$ that describes the fibers orientation for a slice $\boldsymbol{x} = \boldsymbol{x}(\xi_1, \xi_2, \xi_3 = \text{const})$ of the ℓ-th lamina.

In the reference system identified by $\boldsymbol{m}_1^{\langle\ell\rangle}$, $\boldsymbol{m}_2^{\langle\ell\rangle}$ and $\boldsymbol{m}_3^{\langle\ell\rangle}$, the material is assumed to be orthotropic and governed by the constitutive relationship

$$\widetilde{\boldsymbol{\sigma}}^{\langle\ell\rangle} = \widetilde{\boldsymbol{c}}^{\langle\ell\rangle}\widetilde{\boldsymbol{\gamma}}^{\langle\ell\rangle}, \tag{9}$$

where $\widetilde{\boldsymbol{\gamma}}^{\langle\ell\rangle}$ and $\widetilde{\boldsymbol{\sigma}}^{\langle\ell\rangle}$ collects the strain and stress components in the local material reference system according to the Voigt notation and $\widetilde{\boldsymbol{c}}^{\langle\ell\rangle}$ is the 6×6 stiffness matrix of the corresponding elastic coefficients, which are typically given in terms of Young's moduli, shear moduli and Poisson's ratios [1]. Using standard transformation operations [63], Eq.(9) is eventually written as

$$\boldsymbol{\sigma}^{\langle\ell\rangle} = \boldsymbol{c}^{\langle\ell\rangle}\boldsymbol{\gamma}^{\langle\ell\rangle} \tag{10}$$

where $\boldsymbol{\gamma}^{\langle\ell\rangle}$ and $\boldsymbol{\sigma}^{\langle\ell\rangle}$ collect the components of the strain and stress tensors referred to the global Cartesian reference system and $\boldsymbol{c}^{\langle\ell\rangle}$ collects the related coefficients.

2.4. The Equivalent-Single-Layer theory for shells

As introduced in Sec.(1), the present formulation is based on the Equivalent-Single-Layer theory for shells [27, 28], whereby the considered multilayered shell is replaced by a single layer with equivalent properties. The starting point of this approach is the introduction of a suitable expansion of the displacement components in terms of *known* thickness functions and *unknown* in-plane functions. In this work, such an expansion is given for the covariant components u_{ξ_i} of the displacement field as follows:

$$u_{\xi_i}^{\langle\ell\rangle}(\xi_1, \xi_2, \xi_3) = \sum_{k=0}^{N_i} U_{ik}(\xi_1, \xi_2) f_k(\xi_3), \quad \ell = 1, \ldots, N_\ell. \tag{11}$$

In Eq.(11), N_i is the order of the expansion associated to the covariant component u_{ξ_i}, $U_{ik}(\xi_1, \xi_2)$ denotes the unknown in-plane functions, which will also be referred to as *generalized displacement*, and $f_k(\xi_3)$ denotes the known thickness functions, which, for the numerical applications discussed in Sec.(4), will be chosen as the Legendre polynomials scaled in the interval $[-\tau/2, \tau/2]$; however, it is noted that the present formulation does not depend on the specific choice of the thickness functions. It is also worth noting that, consistently with the ESL approach, the the expansion given in Eq.(11) is valid for all the layers of the shells but the expansion order can be assigned independently to each covariant displacement component.

The displacement expansion given in Eq.(11) is conveniently written in matrix form as

$$\boldsymbol{u}_\xi = \boldsymbol{F}(\xi_3)\boldsymbol{U}(\xi_1, \xi_2), \tag{12}$$

where the subscript $\langle\ell\rangle$ has been dropped because the displacement expansion is the same for all the layers, $\boldsymbol{F}(\xi_3)$ is a $3 \times N_U$ matrix containing the thickness functions, $\boldsymbol{U}(\xi_1, \xi_2)$ is a $N_U \times 1$ vector collecting the generalized displacements and $N_U \equiv N_1 + N_2 + N_3 + 3$. Upon substituting Eq.(12) into Eq.(7), it is possible to obtain the expression of the strain $\boldsymbol{\gamma}$ as a function of the introduced thickness and the generalized displacements as follows

$$\boldsymbol{\gamma}^{\langle\ell\rangle} = \boldsymbol{J}_0\boldsymbol{U} + \boldsymbol{J}_\alpha\frac{\partial \boldsymbol{U}}{\partial \xi_\alpha}, \quad \ell = 1, \ldots, N_\ell, \tag{13}$$

where

$$\boldsymbol{J}_0 \equiv \boldsymbol{I}_i\left(\frac{\partial \xi_j}{\partial x_i}\frac{\partial \boldsymbol{R}}{\partial \xi_j}\boldsymbol{F} + \frac{\partial \xi_3}{\partial x_i}\boldsymbol{R}\frac{\mathrm{d}\boldsymbol{F}}{\mathrm{d}\xi_3}\right) \quad \text{and} \quad \boldsymbol{J}_\alpha \equiv \boldsymbol{I}_i\frac{\partial \xi_\alpha}{\partial x_i}\boldsymbol{R}\boldsymbol{F}. \tag{14}$$

Eventually, the vector containing the stress components is obtained by combining Eq.(13) and Eq.(10) as

$$\boldsymbol{\sigma}^{\langle\ell\rangle} = \boldsymbol{c}^{\langle\ell\rangle}\left(\boldsymbol{J}_0\boldsymbol{U} + \boldsymbol{J}_\alpha\frac{\partial\boldsymbol{U}}{\partial\xi_\alpha}\right), \quad \ell = 1,\dots,N_\ell. \tag{15}$$

2.5. Governing equations

The expansion introduced in the preceding section allows to write the mechanical variables of the problem in terms of the unknown generalized displacements collected in the vector $\boldsymbol{U}(\xi_1,\xi_2)$, whose governing equations are derived from the Principle of Virtual Displacements (PVD). For the problem at hand, the PVD is written as

$$\sum_{\ell=1}^{N_\ell}\int_{V^{\langle\ell\rangle}}\delta\boldsymbol{\gamma}^{\langle\ell\rangle\intercal}\boldsymbol{\sigma}^{\langle\ell\rangle}\,\mathrm{d}V = \sum_{\ell=1}^{N_\ell}\int_{V^{\langle\ell\rangle}}\delta\boldsymbol{u}^{\langle\ell\rangle\intercal}\overline{\boldsymbol{b}}^{\langle\ell\rangle}\,\mathrm{d}V + \sum_{\ell=1}^{N_\ell}\int_{S^{\langle\ell\rangle}}\delta\boldsymbol{u}^{\langle\ell\rangle\intercal}\overline{\boldsymbol{t}}^{\langle\ell\rangle}\,\mathrm{d}S \tag{16}$$

where $\overline{\boldsymbol{b}}^{\langle\ell\rangle}$ is a vector containing the Cartesian components of the prescribed volume forces acting throughout the volume of the ℓ-th layer and $\overline{\boldsymbol{t}}^{\langle\ell\rangle}$ is a vector containing the Cartesian components of the prescribed tractions acting on the surface of ℓ-th layer. Upon using Eq.(4) to express $\boldsymbol{u}$ as a function of $\boldsymbol{u}_\xi$ and using Eqs.(3), (12), (13) and (15) into Eq.(16), the following expression of the PVD for the multilayered shell is obtained

$$\int_{\Omega_\xi}\left[\frac{\partial\delta\boldsymbol{U}^\intercal}{\partial\xi_\alpha}\left(\boldsymbol{Q}_{\alpha\beta}\frac{\partial\boldsymbol{U}}{\partial\xi_\beta} + \boldsymbol{R}_{\alpha3}\boldsymbol{U}\right) + \delta\boldsymbol{U}^\intercal\left(\boldsymbol{R}_{\alpha3}^\intercal\frac{\partial\boldsymbol{U}}{\partial\xi_\alpha} + \boldsymbol{S}_{33}\boldsymbol{U}\right)\right]\mathrm{d}\Omega_\xi = \int_{\Omega_\xi}\delta\boldsymbol{U}^\intercal\overline{\boldsymbol{B}}\,\mathrm{d}\Omega_\xi + \int_{\partial\Omega_\xi}\delta\boldsymbol{U}^\intercal\overline{\boldsymbol{T}}\,\mathrm{d}\partial\Omega_\xi. \tag{17}$$

In Eq.(17), $\partial\Omega_\xi$ denotes the contour of Ω_ξ, the matrices $\boldsymbol{Q}_{\alpha\beta}$, $\boldsymbol{R}_{\alpha3}$ and $\boldsymbol{S}_{33}$ are referred to as the generalized stiffness matrices while the vectors $\overline{\boldsymbol{B}}$ and $\overline{\boldsymbol{T}}$ are the generalized domain and boundary loads, respectively. Their expressions are given as follows:

$$\boldsymbol{Q}_{\alpha\beta} \equiv \sum_{\ell=1}^{N_\ell}\int_{\xi_{3b}^{\langle\ell\rangle}}^{\xi_{3t}^{\langle\ell\rangle}}\boldsymbol{J}_\alpha\boldsymbol{c}^{\langle\ell\rangle}\boldsymbol{J}_\beta\sqrt{g}\,\mathrm{d}\xi_3, \tag{18a}$$

$$\boldsymbol{R}_{\alpha3} \equiv \sum_{\ell=1}^{N_\ell}\int_{\xi_{3b}^{\langle\ell\rangle}}^{\xi_{3t}^{\langle\ell\rangle}}\boldsymbol{J}_\alpha\boldsymbol{c}^{\langle\ell\rangle}\boldsymbol{J}_0\sqrt{g}\,\mathrm{d}\xi_3, \tag{18b}$$

$$\boldsymbol{S}_{33} \equiv \sum_{\ell=1}^{N_\ell}\int_{\xi_{3b}^{\langle\ell\rangle}}^{\xi_{3t}^{\langle\ell\rangle}}\boldsymbol{J}_0\boldsymbol{c}^{\langle\ell\rangle}\boldsymbol{J}_0\sqrt{g}\,\mathrm{d}\xi_3, \tag{18c}$$

and

$$\overline{\boldsymbol{B}} \equiv \left(\boldsymbol{F}^\intercal\boldsymbol{R}^\intercal\overline{\boldsymbol{t}}\sqrt{g}\sqrt{n_i g^{ij} n_j}\right)_{\xi_3=\pm\tau/2} + \sum_{\ell=1}^{N_\ell}\int_{\xi_{3b}^{\langle\ell\rangle}}^{\xi_{3t}^{\langle\ell\rangle}}\boldsymbol{F}^\intercal\boldsymbol{R}^\intercal\overline{\boldsymbol{b}}\sqrt{g}\,\mathrm{d}\xi_3, \tag{19a}$$

$$\overline{\boldsymbol{T}} \equiv \sum_{\ell=1}^{N_\ell}\int_{\xi_{3b}^{\langle\ell\rangle}}^{\xi_{3t}^{\langle\ell\rangle}}\boldsymbol{F}^\intercal\boldsymbol{R}^\intercal\overline{\boldsymbol{t}}^{\langle\ell\rangle}\sqrt{g}\sqrt{n_i g^{ij} n_j}\,\mathrm{d}\xi_3. \tag{19b}$$

Eventually, by performing an integration by parts and by resorting to the stationarity of Eq.(17), one obtains the equations governing the elastic response of the ESL shell

$$-\frac{\partial}{\partial\xi_\alpha}\left(\boldsymbol{Q}_{\alpha\beta}\frac{\partial\boldsymbol{U}}{\partial\xi_\beta} + \boldsymbol{R}_{\alpha3}\boldsymbol{U}\right) + \boldsymbol{R}_{\alpha3}^\intercal\frac{\partial\boldsymbol{U}}{\partial\xi_\alpha} + \boldsymbol{S}_{33}\boldsymbol{U} = \overline{\boldsymbol{B}}, \quad \text{in } \Omega_\xi, \tag{20}$$

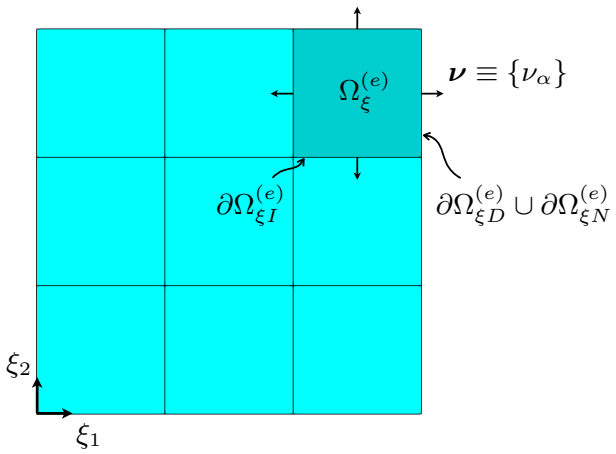

Figure 3: Sample 3×3 mesh of a square domain with a generic element in darker color.

and the following set of boundary conditions

$$\begin{cases} \nu_\alpha \left(\boldsymbol{Q}_{\alpha\beta} \frac{\partial \boldsymbol{U}}{\partial \xi_\beta} + \boldsymbol{R}_{\alpha 3} \boldsymbol{U} \right) = \overline{\boldsymbol{T}}, & \text{on } \partial\Omega_{\xi N} \\ \boldsymbol{U} = \overline{\boldsymbol{U}}, & \text{on } \partial\Omega_{\xi D} \end{cases}, \tag{21}$$

where ν_α is the α-th component of the outer unit normal to the boundary $\partial\Omega_\xi$, $\partial\Omega_{\xi D} \subset \partial\Omega_\xi$ is the part of Ω_ξ where kinematic boundary conditions are prescribed and $\partial\Omega_{\xi N} \subset \partial\Omega_\xi$ is the part of Ω_ξ where mechanical boundary conditions are prescribed.

3. Discontinuous Galerkin framework

As customary in dG formulations [47], the governing equations are rewritten as a system of first-order partial differential equations by introducing an auxiliary variable, which, following Ref.[55], is defined as

$$\boldsymbol{\Sigma}_\alpha \equiv \boldsymbol{Q}_{\alpha\beta} \frac{\partial \boldsymbol{U}}{\partial \xi_\beta} + \boldsymbol{R}_{\alpha 3} \boldsymbol{U}, \tag{22}$$

and allows to replace Eq.(20) with the equivalent set of equations

$$-\frac{\partial \boldsymbol{\Sigma}_\alpha}{\partial x_\alpha} + \boldsymbol{R}_{\alpha 3}^\intercal \frac{\partial \boldsymbol{U}}{\partial \xi_\alpha} + \boldsymbol{S}_{33} \boldsymbol{U} = \overline{\boldsymbol{B}} \tag{23a}$$

$$\boldsymbol{\Sigma}_\alpha = \boldsymbol{Q}_{\alpha\beta} \frac{\partial \boldsymbol{U}}{\partial \xi_\beta} + \boldsymbol{R}_{\alpha 3} \boldsymbol{U}. \tag{23b}$$

The mesh discretization is then introduced and the domain Ω_ξ is subdivided into N_e non-overlapping elements, such that $\Omega_\xi = \cup_e \Omega_\xi^{(e)}$, where $\Omega_\xi^{(e)}$ denotes the domain of the generic e-th element. As an example, Fig.(3) shows a sample 3×3 mesh of a square domain and the generic element $\Omega_\xi^{(e)}$ (in darker color); the figure also shows the element's outer unit normal $\boldsymbol{\nu} \equiv \{\nu_\alpha\}$ and its boundary $\partial\Omega_\xi^{(e)} \equiv \partial\Omega_{\xi I}^{(e)} \cup \partial\Omega_{\xi D}^{(e)} \cup \partial\Omega_{\xi N}^{(e)}$, which consists of the boundary $\partial\Omega_{\xi I}^{(e)}$ that the element shares with its neighboring elements, the boundary $\partial\Omega_{\xi D}^{(e)}$ where kinematic boundary conditions are prescribed and the boundary $\partial\Omega_{\xi N}^{(e)}$ where mechanical boundary conditions are prescribed.

Over each mesh element, Eqs.(23a) and (23b) are stated in weak sense as

$$\int_{\Omega_\xi^{(e)}} \frac{\partial \boldsymbol{V}^\intercal}{\partial \xi_\alpha} \boldsymbol{\Sigma}_{h\alpha} + \boldsymbol{V}^\intercal \left(\boldsymbol{R}_{\alpha 3}^\intercal \frac{\partial \boldsymbol{U}_h}{\partial \xi_\alpha} + \boldsymbol{S}_{33} \boldsymbol{U}_h \right) = \int_{\partial\Omega_\xi^{(e)}} \boldsymbol{V}^\intercal \widehat{\boldsymbol{\Sigma}}_\alpha \nu_\alpha + \int_{\Omega_\xi^{(e)}} \boldsymbol{V}^\intercal \overline{\boldsymbol{B}} \tag{24a}$$

and

$$\int_{\Omega_\xi^{(e)}} \boldsymbol{\Gamma}_\alpha^\intercal \boldsymbol{\Sigma}_{h\alpha} = \int_{\Omega_\xi^{(e)}} \boldsymbol{\Gamma}_\alpha^\intercal \left(\boldsymbol{Q}_{\alpha\beta} \frac{\partial \boldsymbol{U}_h}{\partial \xi_\beta} + \boldsymbol{R}_{\alpha 3} \boldsymbol{U}_h \right) + \int_{\partial\Omega_\xi^{(e)}} (\boldsymbol{\Gamma}_\alpha^\intercal \boldsymbol{Q}_{\alpha\beta} + \boldsymbol{V}^\intercal \boldsymbol{R}_{\beta 3}^\intercal)(\widehat{\boldsymbol{U}} - \boldsymbol{U}_h)\nu_\beta, \tag{24b}$$

respectively, where: $\boldsymbol{\Sigma}_\alpha$ and $\boldsymbol{U}$ have been replaced by their respective numerical approximations $\boldsymbol{\Sigma}_{h\alpha}$ and $\boldsymbol{U}_h$; $\widehat{\boldsymbol{\Sigma}}_\alpha$ and $\widehat{\boldsymbol{U}}$ are the so-called *numerical fluxes*, whose explicit expression will be given in Sec.(3.1); $\boldsymbol{V}$ and $\boldsymbol{\Gamma}_\alpha$ are the test functions taken from the space $\mathcal{V}_{hp}^{N_U}$ of discontinuous vector fields defined as

$$\mathcal{V}_{hp}^{N_U} \equiv \left\{ v : \Omega_\xi \to \mathbb{R} \mid v|_{\Omega_\xi^{(e)}} \in \mathcal{P}_p^{(e)} \ \forall e = 1, ..., N_e \right\}^{N_U}, \tag{25}$$

where $\mathcal{P}_p^{(e)}$ is the space of tensor-product Legendre polynomials with degree p defined over e-th mesh element. It is noted that the basis functions used to express $\boldsymbol{U}_h$ are also taken from $\mathcal{V}_{hp}^{N_U}$; this will lead to a symmetric algebraic system to be solved.

Similarly to the argument regarding the choice of the thickness functions, the present dG formulation does not depend on the specific choice of the function space. In fact, as already mentioned in the Introduction, dG formulations allow to use different numerical approximations within the same mesh since the continuity of the solution is recovered via the boundary terms appearing in Eqs.(24a) and (24b) and involving the numerical fluxes $\widehat{\boldsymbol{\Sigma}}_\alpha$ and $\widehat{\boldsymbol{U}}$, which are discussed in the next section.

3.1. Interior Penalty discontinuous Galerkin scheme

Different choices of $\widehat{\boldsymbol{\Sigma}}_\alpha$ and $\widehat{\boldsymbol{U}}$ leads to different dG formulations [47]. In this work, we employ the Interior Penalty dG formulation proposed by Gulizzi et al.[55, 56, 57], whereby the numerical fluxes at the elements boundary are defined as follows

$$\widehat{\boldsymbol{U}} \equiv \begin{cases} \{\boldsymbol{U}_h\}, & \text{on } \partial\Omega_{\xi I}^{(e)} \\ \overline{\boldsymbol{U}}, & \text{on } \partial\Omega_{\xi D}^{(e)} \\ \boldsymbol{U}_h, & \text{on } \partial\Omega_{\xi N}^{(e)} \end{cases} \tag{26}$$

and

$$\begin{cases} \widehat{\boldsymbol{\Sigma}}_\alpha \equiv \{\boldsymbol{Q}_{\alpha\beta} \frac{\partial \boldsymbol{U}_h}{\partial \xi_\beta} + \boldsymbol{R}_{\alpha 3} \boldsymbol{U}_h\} - \mu [\![\boldsymbol{U}_h]\!]_\alpha, & \text{on } \partial\Omega_{\xi I}^{(e)} \\ \widehat{\boldsymbol{\Sigma}}_\alpha \equiv \boldsymbol{Q}_{\alpha\beta} \frac{\partial \boldsymbol{U}_h}{\partial \xi_\beta} + \boldsymbol{R}_{\alpha 3} \boldsymbol{U}_h - \mu(\boldsymbol{U}_h - \overline{\boldsymbol{U}})\nu_\alpha, & \text{on } \partial\Omega_{\xi D}^{(e)} \\ \nu_\alpha \widehat{\boldsymbol{\Sigma}}_\alpha \equiv \overline{\boldsymbol{T}}, & \text{on } \partial\Omega_{\xi N}^{(e)} \end{cases}. \tag{27}$$

In Eqs.(26) and (27), μ denotes the so-called *penalty parameter* and $\{\bullet\}$ and $[\![\bullet]\!]_\alpha$ are the so-called *average* and *jump* operators, respectively, which are defined at the interface between the elements e and e' as follows

$$\{\bullet\} \equiv \frac{1}{2} \left(\bullet^{(e)} + \bullet^{(e')} \right) \quad \text{and} \quad [\![\bullet]\!]_\alpha \equiv \nu_\alpha^{(e)} \bullet^{(e)} + \nu_\alpha^{(e')} \bullet^{(e')}, \tag{28}$$

being $\nu_\alpha^{(e)}$ the α-th component of outer unit normal to the boundary of the e-th element.

Eventually, upon setting $\boldsymbol{\Gamma}_\alpha \equiv \partial \boldsymbol{V}/\partial\xi_\alpha$, combining Eqs.(24a) and (24b), and summing over all the mesh elements, one obtains the so-called *primal form* of the proposed method:

$$B(\boldsymbol{V},\boldsymbol{U}_h) = F(\boldsymbol{V},\overline{\boldsymbol{B}},\overline{\boldsymbol{T}},\overline{\boldsymbol{U}}) \tag{29}$$

which holds $\forall \boldsymbol{V} \in \mathcal{V}_{hp}^{N_U}$ and where

$$\begin{aligned} B(\boldsymbol{V},\boldsymbol{U}_h) \equiv & \int_{\Omega_h} \frac{\partial \boldsymbol{V}^\intercal}{\partial\xi_\alpha}\left(\boldsymbol{Q}_{\alpha\beta}\frac{\partial \boldsymbol{U}_h}{\partial\xi_\beta} + \boldsymbol{R}_{\alpha 3}\boldsymbol{U}_h\right) + \boldsymbol{V}^\intercal\left(\boldsymbol{R}_{\alpha 3}^\intercal\frac{\partial \boldsymbol{U}_h}{\partial\xi_\alpha} + \boldsymbol{S}_{33}\boldsymbol{U}_h\right) + \\ & - \int_{\partial\Omega_{hI}} [\![\boldsymbol{V}]\!]_\alpha^\intercal\left\{\boldsymbol{Q}_{\alpha\beta}\frac{\partial \boldsymbol{U}_h}{\partial\xi_\beta} + \boldsymbol{R}_{\alpha 3}\boldsymbol{U}_h\right\} + \left\{\frac{\partial \boldsymbol{V}^\intercal}{\partial\xi_\alpha}\boldsymbol{Q}_{\alpha\beta} + \boldsymbol{V}^\intercal\boldsymbol{R}_{\beta 3}^\intercal\right\}[\![\boldsymbol{U}_h]\!]_\beta + \\ & - \int_{\partial\Omega_{hD}} \nu_\alpha \boldsymbol{V}^\intercal\left(\boldsymbol{Q}_{\alpha\beta}\frac{\partial \boldsymbol{U}_h}{\partial\xi_\beta} + \boldsymbol{R}_{\alpha 3}\boldsymbol{U}_h\right) + \left(\frac{\partial \boldsymbol{V}^\intercal}{\partial\xi_\alpha}\boldsymbol{Q}_{\alpha\beta} + \boldsymbol{V}^\intercal\boldsymbol{R}_{\beta 3}^\intercal\right)\boldsymbol{U}_h\nu_\beta + \\ & + \int_{\partial\Omega_{hI}} \mu[\![\boldsymbol{V}]\!]_\alpha^\intercal[\![\boldsymbol{U}_h]\!]_\alpha + \int_{\partial\Omega_{hD}} \mu\boldsymbol{V}^\intercal\boldsymbol{U}_h \end{aligned} \tag{30}$$

and

$$F(\boldsymbol{V},\overline{\boldsymbol{B}},\overline{\boldsymbol{T}},\overline{\boldsymbol{U}}) \equiv \int_{\Omega_h} \boldsymbol{V}^\intercal\overline{\boldsymbol{B}} + \int_{\partial\Omega_{hN}} \boldsymbol{V}^\intercal\overline{\boldsymbol{T}} - \int_{\partial\Omega_{hD}}\left(\frac{\partial \boldsymbol{V}^\intercal}{\partial\xi_\alpha}\boldsymbol{Q}_{\alpha\beta} + \boldsymbol{V}^\intercal\boldsymbol{R}_{\beta 3}^\intercal\right)\overline{\boldsymbol{U}}\nu_\beta + \int_{\partial\Omega_{hD}} \mu\boldsymbol{V}^\intercal\overline{\boldsymbol{U}}. \tag{31}$$

In (30) and (31), the following notation has been used to denote the so-called *broken integrals*:

$$\int_{\Omega_h} \bullet \equiv \sum_{e=1}^{N_e} \int_{\Omega_\xi^{(e)}} \bullet^{(e)}\ \mathrm{d}\Omega_\xi \tag{32a}$$

and

$$\int_{\partial\Omega_{hI}} \bullet \equiv \sum_{e=1}^{N_e} \int_{\partial\Omega_{\xi I}^{(e)}} \bullet^{(e)}\ \mathrm{d}\partial\Omega_\xi, \quad \int_{\partial\Omega_{hD}} \bullet \equiv \sum_{e=1}^{N_e} \int_{\partial\Omega_{\xi D}^{(e)}} \bullet^{(e)}\ \mathrm{d}\partial\Omega_\xi, \quad \int_{\partial\Omega_{hN}} \bullet \equiv \sum_{e=1}^{N_e} \int_{\partial\Omega_{\xi N}^{(e)}} \bullet^{(e)}\ \mathrm{d}\partial\Omega_\xi. \tag{32b}$$

4. Numerical results

In this section, the capabilities of the proposed formulation are assessed through several test cases involving isotropic, orthotropic and multilayered shells in various curved geometric configurations. For each test case, different ESL theories are considered and the theory corresponding to the choice of a specific order of expansion is denoted by $\mathrm{ED}_{N_1N_2N_3}$, where it is recalled that N_i is the order of thickness expansion for the i-th covariant component of the displacement field. The numerical tests are also performed using the FSDT, which is the most commonly employed theory for laminated thin and moderately thick structures and can be considered as a special case of the theory ED_{110} where the stiffness coefficients are modified according to the plane-stress assumption [1, 2].

Five test cases are presented: Secs.(4.1), (4.2) and (4.3) are devoted to the analysis of cylindrical, toroidal and wing-shaped shells, respectively, and refer to geometries that are parametrized via orthogonal curvilinear coordinates; Secs.(4.4) and (4.5) are devoted to the analysis of a planar shell and a generally-shaped shell, respectively, and show examples of geometries that are parametrized

Table 1: Properties of the considered materials.

Material ID	**Property**	**Component**	**Value**
M_1 (Isotropic)	Young's modulus	E	70 GPa
	Poisson's ratio	ν	0.33
M_2 (Orthotropic)	Young's moduli	E_1	100.0 GPa
		E_2, E_3	4.0 GPa
	Poisson's ratios	ν_{23}, ν_{13}, ν_{12}	0.25
	Shear moduli	G_{23}	0.8 GPa
		G_{13}, G_{12}	2.0 GPa
M_3 (Orthotropic)	Young's moduli	E_1	160.0 GPa
		E_2, E_3	20.0 GPa
	Poisson's ratios	ν_{23}, ν_{13}, ν_{12}	0.25
	Shear moduli	G_{23}	4 GPa
		G_{13}, G_{12}	10.0 GPa

Table 2: Properties of the considered shell sections.

Shell ID	**Material**	**Layup**	**Layer(s) thickness**
C_1 (Single-layer)	M_1	$[0]$	1 cm
C_2 (Single-layer)	M_2	$[0]$	1 cm
C_3 (Multilayered)	M_2	$[0/90]_4$	0.125 cm
T_1 (Single-layer)	M_1	$[0]$	1 cm
T_2 (Single-layer)	M_2	$[0]$	1 cm
T_3 (Multilayered)	M_2	$[0/90]_2$	0.25 cm
W_1 (Single-layer)	M_1	$[0]$	1 cm
W_3 (Multilayered)	M_3	$[0/90]_s$	0.25 cm
P_2 (Single-layer)	M_2	$[0]$	1 cm
P_3 (Multilayered)	M_2	$[0/90/0/90]_s$	0.125 cm
G_1 (Single-layer)	M_1	$[0]$	1 cm

Table 3: Quantities entering the parametric equation of the considered shell mean surfaces.

Cylinder		**Torus**		**Wing**		**Planar shell**		**Generally-curved shell**	
R_c	1 m	R_{1t}	2 m	x_w	0.1 m	b_m	0.5 m	a_g	2 m
θ_c	$\pi/4$	R_{2t}	0.5 m	y_w	0 m	l_m	0.5 m	b_g	1 m
L_c	1 m	θ_{1t}	$\pi/8$	L_{wa}	10 m			f_g	0.44
		θ_{2t}	$\pi/2$	L_{wb}	20 m			Δ_g	4.0
				R_w	1.1 m			L_g	8 m

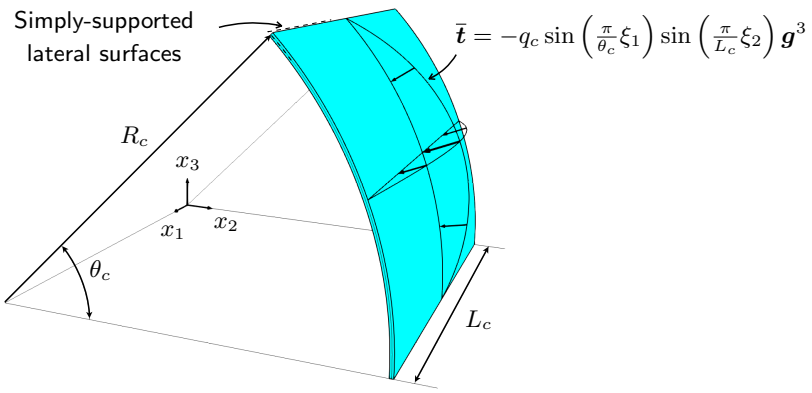

Figure 4: Geometry, boundary conditions and load conditions of the considered cylindrical shell.

via non-orthogonal curvilinear coordinates. The materials considered for the numerical tests are grouped and reported in Tab.(1), the properties of the considered shell sections are reported in Tab.(2) and the parameters entering the equations of shell mean surfaces are given in Tab.(3). All the numerical tests are performed using a structured grid to discretize the shell reference domain Ω_ξ.

As a last general remark on the numerical tests, it is worth stressing that the Interior Penalty formulation requires the introduction of a penalty parameter μ, which appears in the definition of the numerical flux $\widehat{\boldsymbol{\Sigma}}_\alpha$ in Eq.(27) and in the bilinear form given in Eq.(30). Its effect on the numerical solution is similar to what has been observed in previous works on Interior Penalty dG methods for multilayered plates [55] and such an investigation is not reported in this paper for the sake of conciseness. However, following previous observations [55], μ has been chosen as $\mu \sim E/h$, being E a characteristic stiffness of the considered shell and h a characteristic size of the mesh elements. Such a choice is typical in Interior Penalty formulations to ensure optimal convergence [47].

4.1. Cylindrical shell

In the first set of tests, the cylindrical shell shown in Fig.(4) is considered. The mean surface of the shell is described by the equation

$$\boldsymbol{x}_0 = \begin{bmatrix} \xi_2 \\ R_c \cos(\xi_1) \\ R_c \sin(\xi_1) \end{bmatrix} \tag{33}$$

where $\xi_1 \in [0, \theta_c]$, $\xi_2 \in [0, L_c]$ and R_c, θ_c and L_c are reported in the first column of Tab.(3). The shell is subjected to simply supported boundary conditions, which are prescribed in terms of generalized displacements as

$$\begin{cases} \overline{U}_{2k} = 0, & \text{for } k = 0, \dots, N_2 \\ \overline{U}_{3k} = 0, & \text{for } k = 0, \dots, N_3 \end{cases} \text{, at } \xi_1 = 0, \theta_c, \quad \text{and} \quad \begin{cases} \overline{U}_{1k} = 0, & \text{for } k = 0, \dots, N_1 \\ \overline{U}_{3k} = 0, & \text{for } k = 0, \dots, N_3 \end{cases} \text{, at } \xi_2 = 0, L_c. \tag{34}$$

The contribution to the vector $\overline{\boldsymbol{T}}$ of the generalized boundary loads is zero, whereas the only contribution to the vector $\overline{\boldsymbol{B}}$ of the generalized domain loads is given by the traction applied on the top surface of the shell as

$$\bar{\boldsymbol{t}} = -q_c \sin\left(\frac{\pi}{\theta_c}\xi_1\right) \sin\left(\frac{\pi}{L_c}\xi_2\right) \boldsymbol{g}^3, \quad \text{at } \xi_3 = \tau_c/2, \tag{35}$$

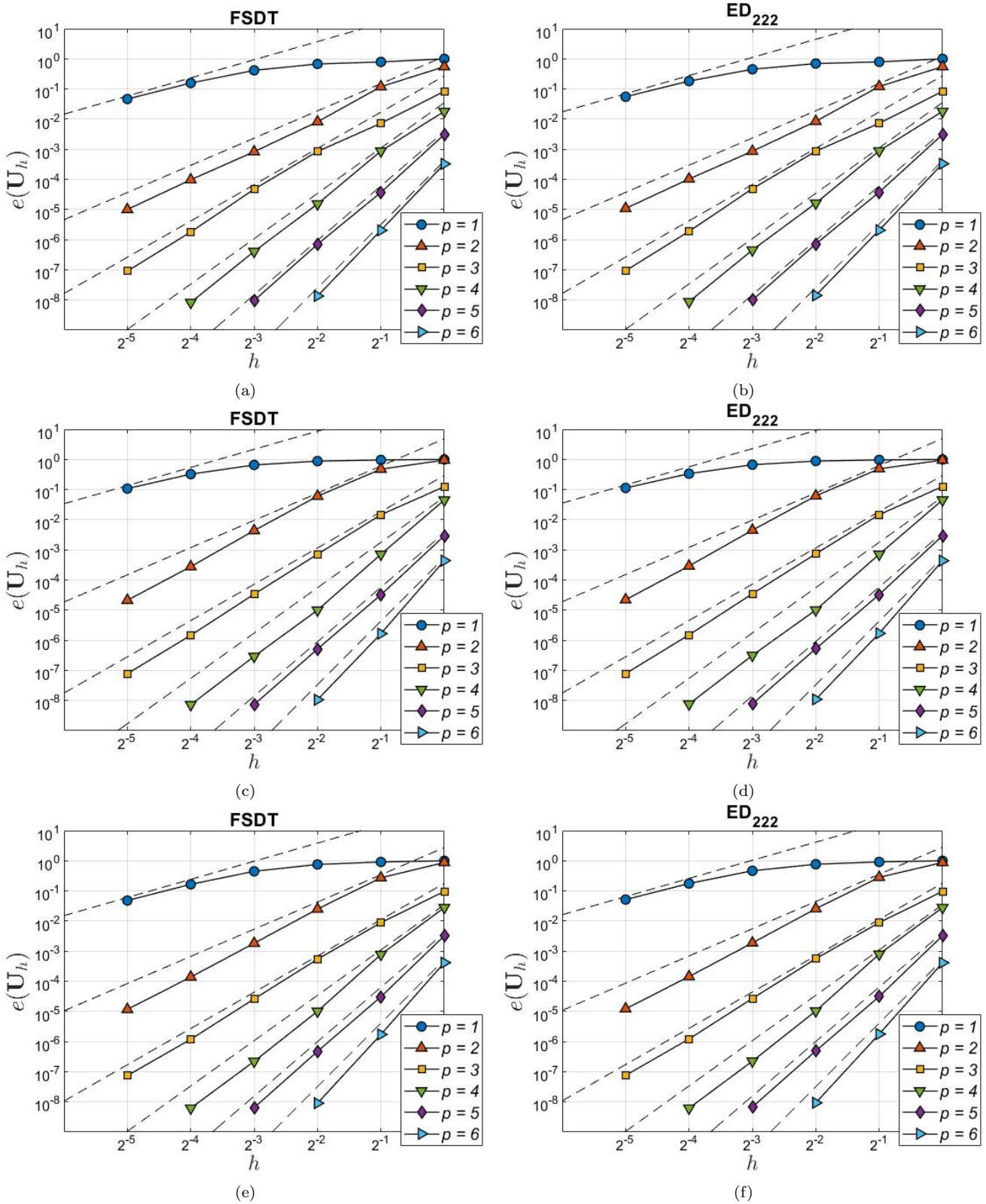

Figure 5: *hp*-convergence analysis for the cylindrical shells shown in Fig.(4). The figures in the left and the right columns refer to the FSDT and the ED_{222} theory, respectively, whereas, from top to bottom, the figures refer to the shell sections C_1, C_2 and C_3 reported in Tab.(2). The slope of the dashed lines is $p+1$.

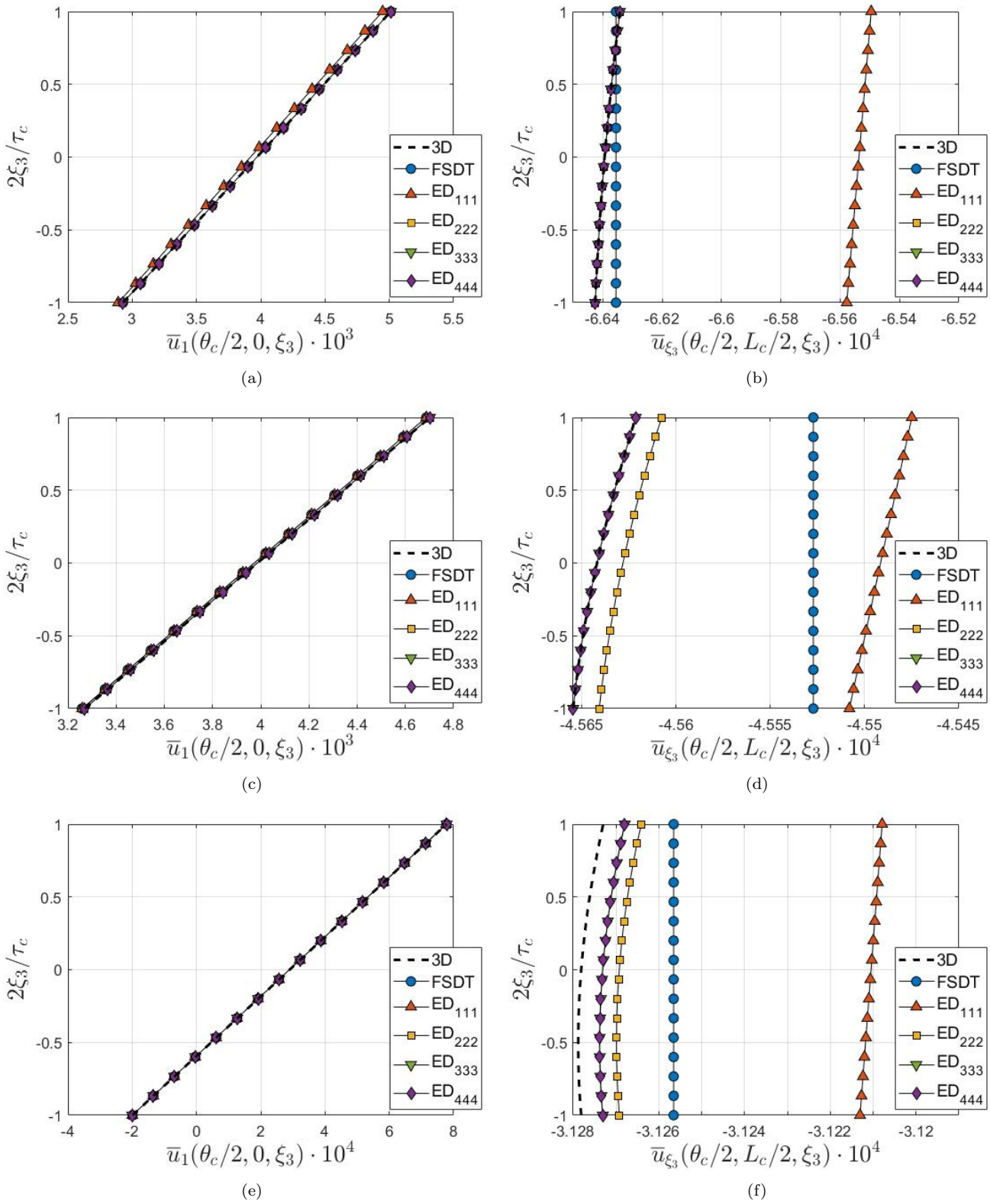

Figure 6: Comparison between the 3D solution and the solution obtained with the present formulation and different shell theories for the cylindrical shells shown in Fig.(4).

where $q_c = 10$ MPa and τ_c is the thickness of the cylindrical shell. As regards the material properties and the stacking sequences, the three shell sections denoted by C_1, C_2 and C_3 in Tab.(2) are considered. It is noted that they all have the same thickness. These settings have been chosen because they admit exact two-dimensional Navier solutions [2] and allow to compute the solution of the corresponding three-dimensional elasticity problem [8].

The reference domain Ω_ξ of the shell is subdivided into $n \times n$ rectangular elements such that the dimensions of each element is $h\theta_c \times hL_c$, being $h \equiv 1/n$ a measure of the element size. Given the existence of the Navier solutions, the following error measure is introduced

$$e(\boldsymbol{U}_h) \equiv \frac{|\boldsymbol{U}_h - \boldsymbol{U}_{\text{ref}}|_\infty}{|\boldsymbol{U}_{\text{ref}}|_\infty}, \tag{36}$$

where $\boldsymbol{U}_h$ is the solution computed using the present Interior Penalty formulation, $\boldsymbol{U}_{\text{ref}}$ is the exact Navier solution and $|\bullet|_\infty$ is the ∞-norm defined over Ω_ξ. Figure (5) shows the hp-convergence analyses in terms of the error given in Eq.(36) as a function of the element size h and the polynomial order p. As it is possible to notice, the present formulation allows to obtain optimal convergence for all the tested shell sections and shell theories.

The solution obtained using the present formulation with a 4×4 mesh, $p = 6$ and the theories FSDT, ED_{111}, ED_{222}, ED_{333}, ED_{444} is then compared with the corresponding solution of three-dimensional elasticity [8]. The comparison is reported in Fig.(6) in the terms of the non-dimensional through-the-thickness Cartesian displacement component $\overline{u}_1$ and curvilinear covariant component $\overline{u}_{\xi_3}$ defined as

$$\overline{u}_1 \equiv u_1 \cdot \left(\frac{\tau_c^2 E_2}{L_c^3 q_c}\right) \quad \text{and} \quad \overline{u}_{\xi_3} \equiv u_{\xi_3} \cdot \left(\frac{\tau_c^3 E_2}{L_c^4 q_c}\right). \tag{37}$$

The top, center and bottom rows of Fig.(6) refer to the isotropic shell C_1, the orthotropic shell C_2 and the laminated shell C_3, respectively, and show that the differences between the 3D solution and the ESL theories are more pronounced for the covariant component $\overline{u}_{\xi_3}$ rather than the Cartesian component $\overline{u}_1$. More specifically regarding $\overline{u}_{\xi_3}$, fig.(6b) shows that all the considered ESL theories with the exception of the ED_{111} are able to recover the 3D solution, fig.(6d) shows that the ESL theories ED_{333} and ED_{444} are able to fully recover the 3D solution and, eventually, fig.(6f) shows that, although the theories ED_{333} and ED_{444} provide a converged ESL solution, ESL theories are not able to fully recover the 3D solution. The obtained results are consistent with the findings reported in Ref.[55] for multilayered plates and, as expected, show that higher-order theories provide a better response than low-order theories when employed for orthotropic and laminated shells. They also suggest that layer-wise theories are generally required to fully recover the 3D solution in laminated structures.

4.2. Toroidal shell

In the second set of tests, the toroidal shell shown in Fig.(7) is considered. The mean surface of the shell is described by the equation

$$\boldsymbol{x}_0 = \begin{bmatrix} \cos(\xi_1)(R_{1t} + R_{2t}\cos(\xi_2)) \\ \sin(\xi_1)(R_{1t} + R_{2t}\cos(\xi_2)) \\ R_{2t}\sin(\xi_2) \end{bmatrix} \tag{38}$$

where $\xi_1 \in [-\theta_{1t}, \theta_{1t}]$, $\xi_2 \in [-\theta_{2t}, \theta_{2t}]$ and R_{1t}, R_{2t}, θ_{1t} and θ_{2t} are reported in the second column of Tab.(3).

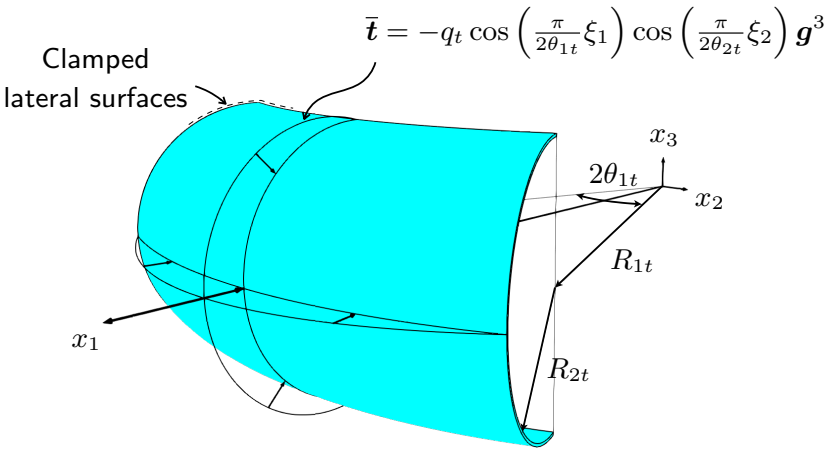

Figure 7: Geometry, boundary conditions and load conditions of the considered toroidal shell.

The shell is subjected to clamped boundary conditions, i.e. $\boldsymbol{U} = \boldsymbol{0}$ for $\{\xi_1, \xi_2\} \in \partial\Omega_\xi$, and to surface tractions over its top surface prescribed as

$$\bar{\boldsymbol{t}} = -q_t \cos\left(\frac{\pi}{2\theta_{1t}}\xi_1\right)\cos\left(\frac{\pi}{2\theta_{2t}}\xi_2\right)\boldsymbol{g}^3, \quad \text{at } \xi_3 = \tau_t/2, \tag{39}$$

where $q_t = 100$ MPa and τ_t is the shell thickness. The considered material properties and the stacking sequences are those of the three shell sections denoted by T_1, T_2 and T_3 in Tab.(2).

Analytical solutions are not available for these tests. Therefore, the solution obtained using the present formulation is compared with the solution computed using the FEM software Abaqus [64]. The comparison is performed in terms of the non-dimensional covariant component $\overline{u}_{\xi_3}$, defined as

$$\overline{u}_{\xi_3} \equiv u_{\xi_3} \cdot \left(\frac{\tau_t^3 E_2}{R_{2t}^4 q_t}\right), \tag{40}$$

versus the number of total degrees of freedom of the algebraic system to be solved. Figures (8a), (8c) and (8e) show $\overline{u}_{\xi_3}$ evaluated at $\{\xi_1, \xi_2, \xi_3\} = \{0, 0, \tau_t/2\}$ using the present formulation with the FSDT and a polynomial order $p = 3$ and using Abaqus' S4R elements for the shell sections T_1, T_2 and T_3, respectively. Similarly, Figs.(8b), (8d) and (8e) show $\overline{u}_{\xi_3}$ evaluated at $\{\xi_1, \xi_2, \xi_3\} = \{0, 0, \tau_t/2\}$ using the present formulation with the ESL theory ED_{222} and a polynomial order $p = 3$ and the results obtained using Abaqus' C3D8R elements for the shell sections T_1, T_2 and T_3, respectively. From the figures, it is possible to note that the present formulation reproduces the FEM results and, when using the ED_{222}, offers a significant saving in terms of total number of degrees of freedom with respect to the 3D model.

4.3. Wing-shaped shell

In set of tests discussed in this section, the wing-shaped shell shown in Fig.(9) is considered. The profile of the wing is generated by means of a Joukowsky transformation [65] and the mean surface of the shell is described by the equation

$$\boldsymbol{x}_0 = \begin{bmatrix} \xi_2 \\ (R_w\cos(\xi_1) - x_w)(1 + 1/\phi(\xi_1)) \\ (R_w\sin(\xi_1) + y_w)(1 - 1/\phi(\xi_1)) \end{bmatrix}, \quad \text{with} \quad \phi(\xi_1) \equiv x_w^2 + y_w^2 + 2R_w(-x_w\cos(\xi_1) + y_w\sin(\xi_1)) + R_w^2, \tag{41}$$

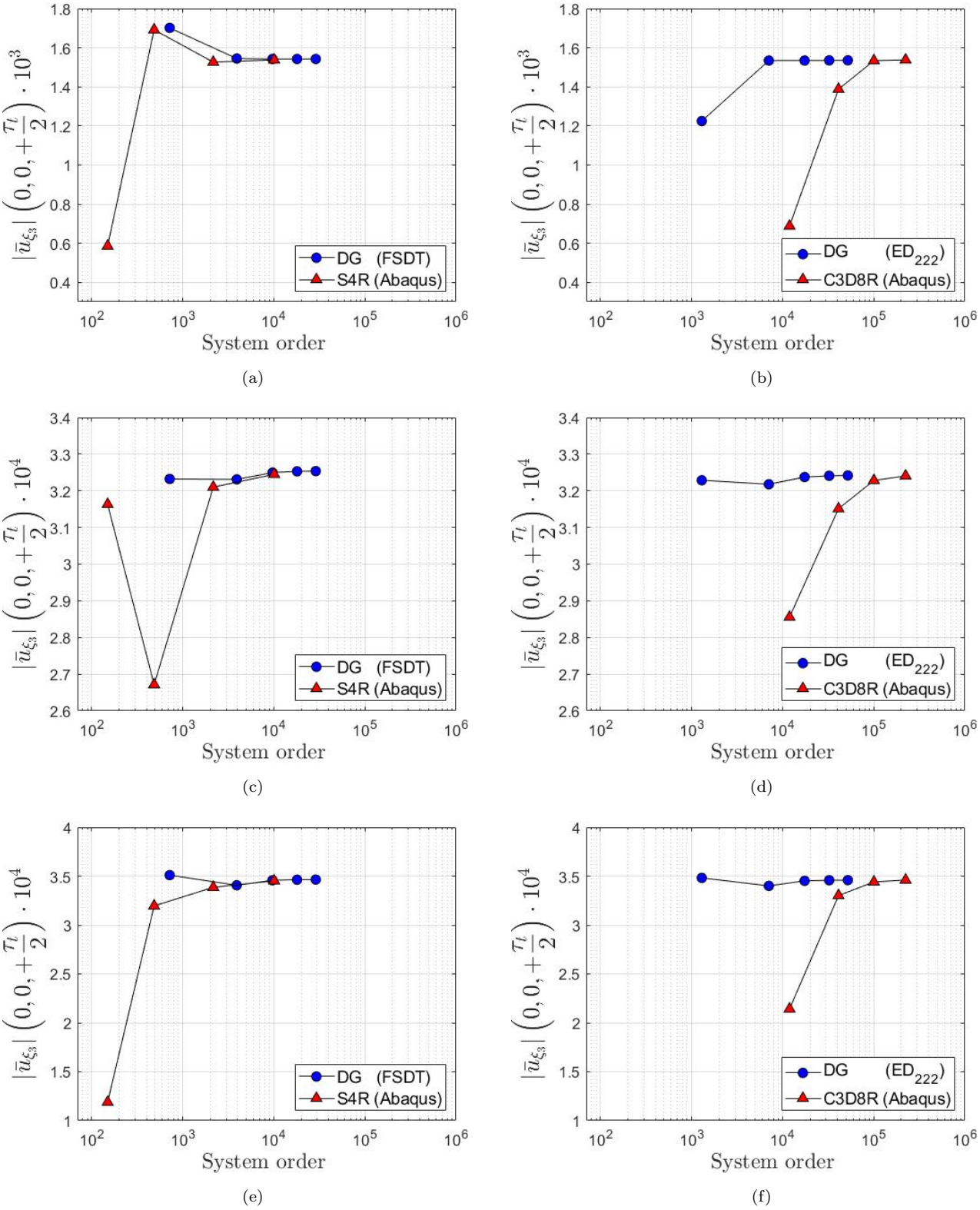

Figure 8: Comparison between the results obtained with the present formulation and the results obtained with FEM for the toroidal shell shown in Fig.(7).

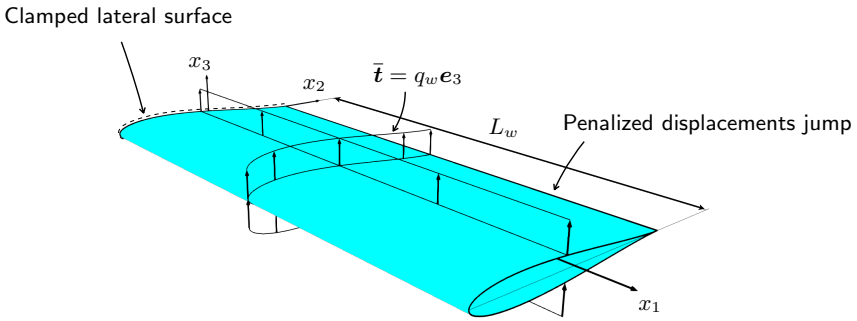

Figure 9: Geometry, boundary conditions and load conditions of the considered wing-shaped shell.

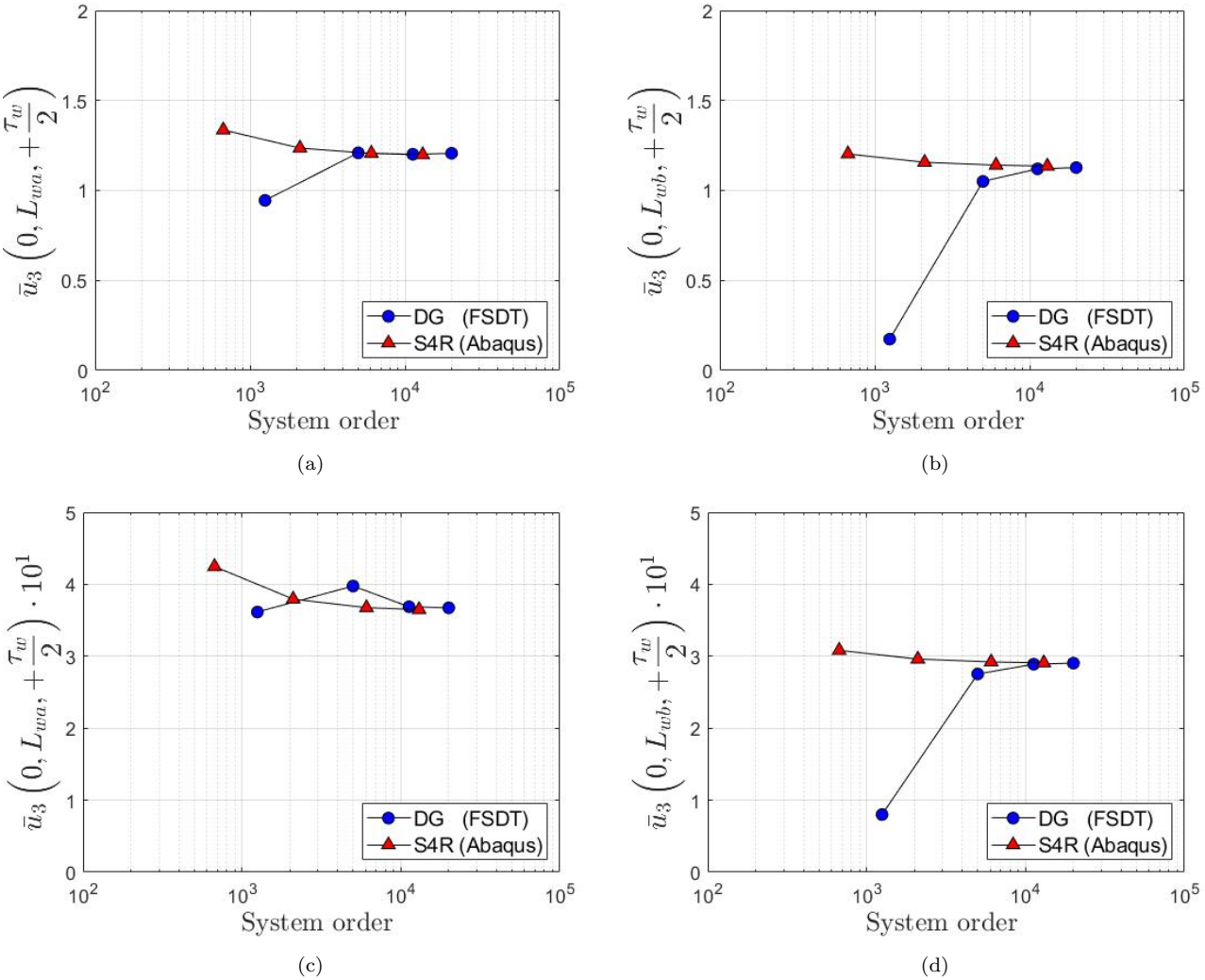

Figure 10: Comparison between the FEM solution and the solution obtained by the present formulation for the wing-shaped shell shown in Fig.(9).

where $\xi_1 \in [0, 2\pi]$, $\xi_2 \in [0, L_w]$, being L_w equal to L_{wa} or L_{wb} whether a short wing or a slender wing is considered, and x_w, y_w, L_{wa}, L_{wb} and R_w are reported in the third column of Tab.(3). As sketched in Fig.(9), the shell is clamped over the lateral surface identified by the points $\boldsymbol{x} = \boldsymbol{x}(\xi_1, \xi_2 = 0, \xi_3)$ and is subjected to prescribed traction $\overline{\boldsymbol{t}} = q_w \boldsymbol{e}_3$ on the outer surface, i.e. the surface identified by $\boldsymbol{x} = \boldsymbol{x}(\xi_1, \xi_2, \xi_3 = \tau_w/2)$, being $\boldsymbol{e}_3 \equiv \{0, 0, 1\}$, $q_w = 10$ kPa and τ_w the thickness of the shell. The remaining surfaces are traction-free.

Eventually, the parametrization of the shell given by Eq.(41) is such that $\boldsymbol{x}_0(\xi_1, \xi_2 = 0) = \boldsymbol{x}_0(\xi_1, \xi_2 = 2\pi)$, i.e. the mean surface is a closed surface, albeit non-smooth at $\xi_2 = 0$ and $\xi_2 = 2\pi$. Therefore, to enforce the displacement continuity at the trailing edge of the wing, the Interior Penalty scheme given in Eq.(29) is supplemented with a term the penalizes the jump between the Cartesian components of the displacement field evaluated at $\boldsymbol{x}_0 = \boldsymbol{x}_0(\xi_1, \xi_2 = 0)$ and the Cartesian components of the displacement field evaluated at $\boldsymbol{x}_0 = \boldsymbol{x}_0(\xi_1, \xi_2 = 2\pi)$. It is worth noting that such an approach has been employed to study assemblies of plates and shells, see e.g. [60, 61, 7] and has been implemented only for this specific test case to show the flexibility of the proposed formulation. A general treatment regarding the assembly of multilayered shells modelled using the present ESL approach is outside the scope of this work and will be considered in future studies.

The two shell sections denoted by W_1 and W_3 in Tab.(2) are considered and the results obtained with the present formulation are compared with those obtained using FEM. The comparison is performed in terms of the non-dimensional Cartesian component versus the number of total degrees of freedom of the algebraic system to be solved; $\overline{u}_3$ is defined as

$$\overline{u}_3 \equiv u_3 \cdot \left(\frac{\tau_w s_w^2 E_2}{L_w^4 q_w} \right), \tag{42}$$

where $s_w = 0.475$ m represents the thickness of the wing profile. All numerical tests investigated in this section are performed using the FSDT. Figures (10a) and (10c) refer to the case of the short wing, i.e. $L_w = L_{wa}$, and show $\overline{u}_3$ evaluated at $\{\xi_1, \xi_2, \xi_3\} = \{0, L_{wa}, \tau_w/2\}$ using the present formulation with polynomial order $p = 4$ and using Abaqus' S4R elements for the shell sections W_1 and W_3, respectively. Similarly, Figs.(10b) and (10d) refer to the case of the slender wing, i.e. $L_w = L_{wb}$, and show $\overline{u}_3$ evaluated at $\{\xi_1, \xi_2, \xi_3\} = \{0, L_{wb}, \tau_w/2\}$ using the present formulation with polynomial order $p = 4$ and using Abaqus' S4R elements for the shell sections W_1 and W_3, respectively. In all cases, it is possible to note that the present formulation reproduces the FEM results.

4.4. Planar elasticity using non-orthogonal curvilinear coordinates

To test a case of a geometry described by a set of non-orthogonal curvilinear coordinates, let us consider the planar geometry shown in Fig.(11) and described by the equation

$$\boldsymbol{x} = \begin{bmatrix} 2\xi_1 \cos(\xi_2) \\ \xi_1 \sin(\xi_2) \\ 0 \end{bmatrix}, \tag{43}$$

where $\xi_1 \in [b_m, b_m + l_m]$, $\xi_2 \in [0, \pi/2]$ and b_m and l_m are reported in the fourth column of Tab.(3). For this case, $\boldsymbol{g}_1 \cdot \boldsymbol{g}_2 \neq 0$. Let us also assume that the domain is subjected to a constant strain $\boldsymbol{\gamma}_{\mathrm{ref}} = \{\varepsilon, -\varepsilon, 0, 0, 0, 0\}^\intercal$, with $\varepsilon = 0.01$, generated by a displacement field whose Cartesian components are $\boldsymbol{u}_{\mathrm{ref}} = \varepsilon\{x_1, -x_2, 0\}^\intercal$. Using Eq.(4), the corresponding covariant components of this displacement field are given as

$$\boldsymbol{u}_{\xi,\mathrm{ref}} = \varepsilon \left\{ \begin{array}{c} -\xi_1(5\sin^2(\xi_2) - 4) \\ -5\xi_1^2 \sin(2\xi_2)/2 \\ 0 \end{array} \right\}. \tag{44}$$

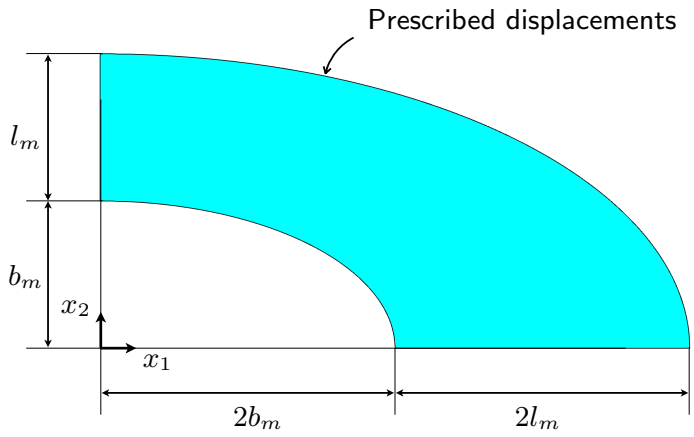

Figure 11: Geometry and boundary conditions of the considered planar shell parametrized using a system of non-orthogonal curvilinear coordinates.

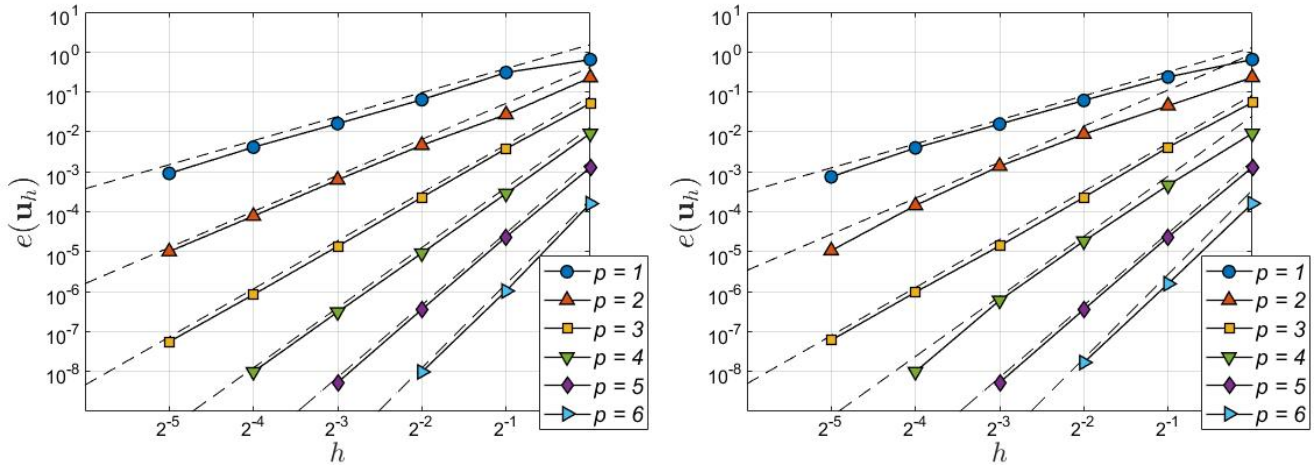

(a) (b)

Figure 12: *hp*-convergence analysis for the planar domain shown in Fig.(11). Figure (a) and (b) respectively refer to the shell sections P_2 and P_3 reported in Tab.(2). The slope of the dashed lines is $p + 1$.

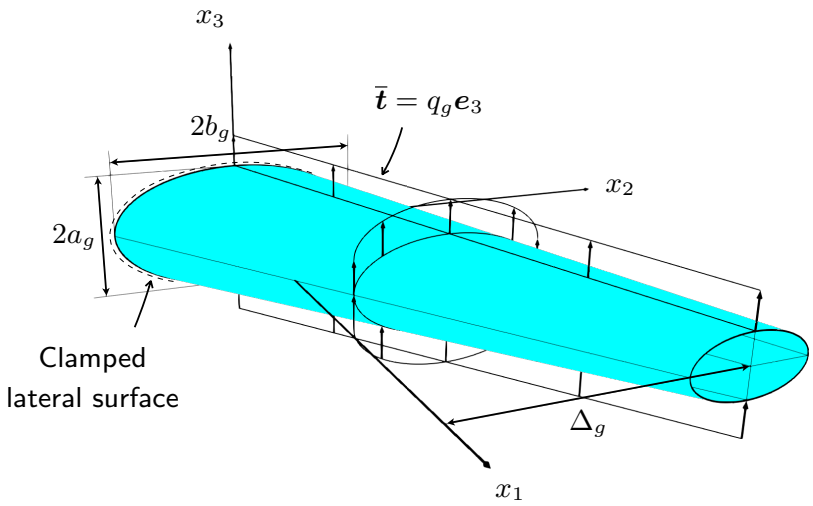

Figure 13: Geometry, boundary conditions and load conditions of the considered generally-curved shell.

Then, the problem considered in this section consists of solving Eq.(20) subjected to the boundary conditions given in Eq.(21) where: $\boldsymbol{U}$ contains the zero-th order generalized displacements only, i.e. $\boldsymbol{U} \equiv \{U_{10}, U_{20}, U_{30}\}^\intercal$, since the out-of-plane behavior is disregarded in this case, and the boundary conditions are prescribed as $\boldsymbol{U} = \overline{\boldsymbol{U}} = \boldsymbol{u}_{\xi,\text{ref}}$. The considered shell sections are those denoted by P_2 and P_3 in Tab.(2), and, for this case, the angle $\theta^{\langle \ell \rangle}$ is referred to the Cartesian reference system rather than the curvilinear reference system.

The modelling domain Ω_ξ of the shell is divided into $n \times n$ elements such that the dimension of each element is $hl_m \times h\pi/2$, being $h \equiv 1/n$ a measure of the element size. The following error measure $e(\boldsymbol{u}_h)$ is introduced

$$e(\boldsymbol{u}_h) \equiv \frac{|\boldsymbol{u}_h - \boldsymbol{u}_{\text{ref}}|_\infty}{|\boldsymbol{u}_{\text{ref}}|_\infty}, \tag{45}$$

where $\boldsymbol{u}_h$ collects the Cartesian components of the displacement field computed with the present formulation. Figure (12) shows $e(\boldsymbol{u}_h)$ as a function of the element size h and the polynomial order p for the two considered shell sections. As it can be noted from the figures, the present formulation offers optimal convergence also when a system of non-orthogonal curvilinear coordinates is employed.

4.5. Generally-curved shell

In the last set of tests, the shell shown in Fig.(13) is considered. The shell consists of a tapered elliptical cylinder swept toward the x_2 axis. Its mean surface is described by the equation

$$\boldsymbol{x}_0 = \begin{bmatrix} \xi_2 \\ a_g \cos(\xi_1)((f_g - 1)\xi_2/L_g + 1) + \Delta_g \xi_2/L_g \\ b_g \sin(\xi_1)((f_g - 1)\xi_2/L_g + 1) \end{bmatrix} \tag{46}$$

where $\xi_1 \in [0, 2\pi]$, $\xi_2 \in [0, L_g]$ and a_g, b_g, f_g, Δ_g and L_g are reported in the fifth column of Tab.(3). The considered shell section is the one denoted by G_1 in Tab.(2). The shell is subjected to clamped boundary conditions on the lateral surface identified by $\boldsymbol{x} = \boldsymbol{x}(\xi_1, \xi_2 = 0, \xi_3)$ and to prescribed tractions $\bar{\boldsymbol{t}} = q_g \boldsymbol{e}_3$ on its outer surface, i.e. the surface identified by $\boldsymbol{x} = \boldsymbol{x}(\xi_1, \xi_2, \xi_3 = \tau_g/2)$, being $\boldsymbol{e}_3 \equiv \{0, 0, 1\}^\intercal$, $q_g = 1$ MPa and τ_g the thickness of the shell; the remaining surfaces are traction-free. Moreover, similarly to the case of the wing-shaped shell, the parametrization given

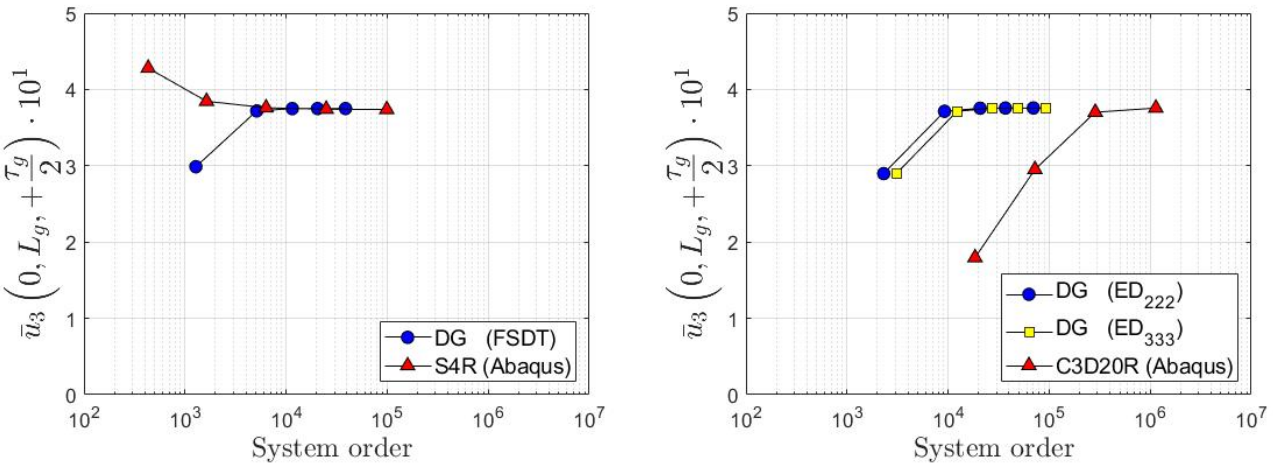

(a) (b)

Figure 14: Comparison between the FEM solution and the solution obtained by the present formulation for the shell shown in Fig.(13).

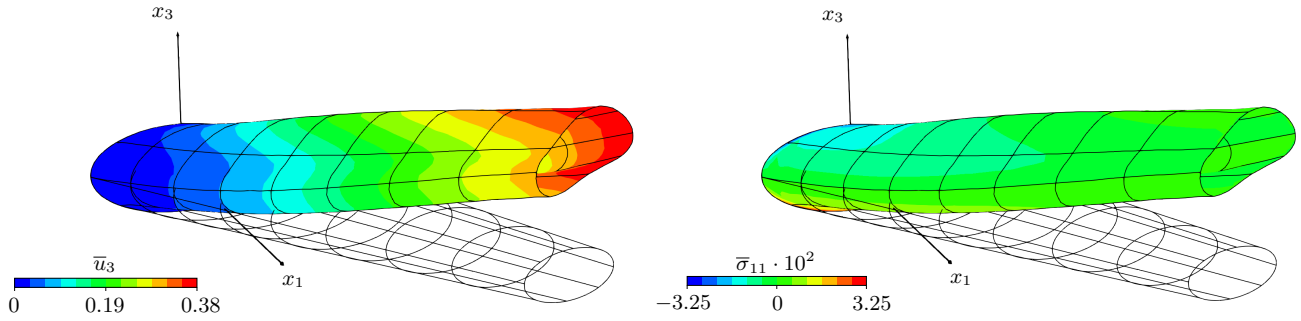

(a) (b)

Figure 15: Deformed shaped of the generally-curved shell problem shown in Fig.(13) with superimposed contours of (a) the displacement component $\overline{u}_3$ and (b) the stress component $\overline{\sigma}_{11}$.

by Eq.(46) describes a closed surface such that $\boldsymbol{x}(\xi_1 = 0, \xi_2, \xi_3) = \boldsymbol{x}(\xi_1 = 2\pi, \xi_2, \xi_3)$. However, in this case, the geometry is smooth and the present formulation can be employed without the need for adding any additional penalization term provided that the domain Ω_ξ is considered periodic in the variable ξ_1.

The results obtained using the present formulation are compared with the results computed using the FEM software Abaqus. The comparison is performed in terms of the non-dimensional Cartesian component $\overline{u}_3$, defined as

$$\overline{u}_3 \equiv u_3 \cdot \left(\frac{\tau_g b_g^2 E_2}{L_g^4 q_g} \right), \tag{47}$$

versus the number of total degrees of freedom of the algebraic system to be solved.

Figures (14a) shows $\overline{u}_3$ evaluated at $\{\xi_1, \xi_2, \xi_3\} = \{0, L_g, \tau_g/2\}$ using the present formulation with the FSDT and a polynomial order $p = 7$ and using Abaqus' S4R elements. Similarly, Fig.(14b) show $\overline{u}_3$ evaluated at $\{\xi_1, \xi_2, \xi_3\} = \{0, L_g, \tau_g/2\}$ using the present formulation with the ESL theories ED_{222} and ED_{333} and using Abaqus' C3D20R elements. Consistently with the findings related to all the previous tests, the figures show that the present formulation reproduces well the FEM results and offers a significant saving in terms of the total number of degrees of freedom.

For the sake of completeness, Figs.(15a) and (15b) show the contour plots of the displacement component $\overline{u}_3$ and the stress component $\overline{\sigma}_{11}$, respectively, which have been computed using the present formulation with a 8×8 mesh of the reference domain Ω_ξ and a polynomial order $p = 7$. In the figures, $\overline{u}_3$ is given by Eq.(47) whereas $\overline{\sigma}_{11} \equiv \sigma_{11} \cdot \left(\frac{\tau_g b_g}{L_g^2 q_g} \right)$.

5. Conclusions

In this work, we presented a high-order formulation for modelling multilayered shells based on Equivalent-Single-Layer theories and the Interior Penalty discontinuous Galerkin method. The ESL approach consists of expressing the covariant components of the displacement field as a series of generalized displacements throughout the thickness of the shell, which in turn is replaced by a layer of equivalent mechanical properties governed by a set of 2D partial differential equations in the curvilinear coordinates. A numerical scheme for the solution of these equations was then developed using the Interior Penalty dG formulation whereby the unknown fields are approximated via discontinuous basis functions and inter-element continuity and boundary conditions are enforced by suitably defined boundary integrals. The combined use of these approaches allowed a high-order representation of the mechanical fields throughout both the shell thickness and the shell modelling domain.

Numerical tests were performed on isotropic, orthotropic and multilayered shells with different geometrical configurations and boundary conditions described by either orthogonal or non-orthogonal curvilinear coordinates. Several shell theories were considered, including the FSDT as a special case. The comparison between the results obtained with the proposed formulation and the results computed using exact or finite element solutions confirmed the accuracy of the proposed approach and also showed that using higher-order two-dimensional theories instead of low-order three-dimensional models leads to significant computational savings in terms of the overall number of degrees of freedom.

Acknowledgements

G.G. and A.M. acknowledge the support of the *Italian Ministry of Education, University and Research* – MIUR – through the project DEVISU, funded under the scheme PRIN-2107 – Grant

22017ZX9X4K_006.

References

[1] R. Jones, Mechanics Of Composite Materials, Materials Science and Engineering Series, Taylor & Francis, 1998.

[2] J. N. Reddy, Mechanics of laminated composite plates and shells: theory and analysis, CRC press, 2003.

[3] J. Reddy, Theory and Analysis of Elastic Plates and Shells, Series in Systems and Control, CRC Press, 2006.

[4] F. A. Fazzolari, M. Viscoti, R. Dimitri, F. Tornabene, 1d-hierarchical ritz and 2d-gdq formulations for the free vibration analysis of circular/elliptical cylindrical shells and beam structures, Composite Structures (2020) 113338.

[5] M. Amabili, J. Reddy, The nonlinear, third-order thickness and shear deformation theory for statics and dynamics of laminated composite shells, Composite Structures (2020) 112265.

[6] M. Petrolo, E. Carrera, Methods and guidelines for the choice of shell theories, Acta Mechanica (2020) 1–40.

[7] G. Sciascia, V. Oliveri, A. Milazzo, P. M. Weaver, Ritz solution for transient analysis of variable-stiffness shell structures, AIAA Journal 58 (4) (2020) 1796–1810.

[8] J. Ren, Analysis of simply-supported laminated circular cylindrical shell roofs, Composite structures 11 (4) (1989) 277–292.

[9] T. Varadan, K. Bhaskar, Bending of laminated orthotropic cylindrical shells—an elasticity approach, Composite Structures 17 (2) (1991) 141–156.

[10] S. Brischetto, Exact three-dimensional static analysis of single-and multi-layered plates and shells, Composites Part B: Engineering 119 (2017) 230–252.

[11] R. Li, X. Zheng, Y. Yang, M. Huang, X. Huang, Hamiltonian system-based new analytic free vibration solutions of cylindrical shell panels, Applied Mathematical Modelling 76 (2019) 900–917.

[12] V. G. Kirchhoff, Über das gleichgewicht und die bewegung einer elastischen scheibe, Journal fur die reine und angewandte Mathematik 40 (1850) 51–88.

[13] P. M. Naghdi, R. P. Nordgren, On the nonlinear theory of elastic shells under the kirchhoff hypothesis, Quarterly of Applied Mathematics 21 (1) (1963) 49–59.

[14] M. W. Johnson, E. Reissner, On the foundations of the theory of thin elastic shells, Journal of Mathematics and Physics 37 (1-4) (1958) 371–392.

[15] J. Reddy, C. Liu, A higher-order shear deformation theory of laminated elastic shells, International journal of engineering science 23 (3) (1985) 319–330.

[16] J. Reddy, A general non-linear third-order theory of plates with moderate thickness, International Journal of Non-Linear Mechanics 25 (6) (1990) 677–686.

[17] R. A. Arciniega, J. Reddy, Consistent third-order shell theory with application to composite cylindrical cylinders, AIAA journal 43 (9) (2005) 2024–2038.

[18] R. Arciniega, J. Reddy, Tensor-based finite element formulation for geometrically nonlinear analysis of shell structures, Computer Methods in Applied Mechanics and Engineering 196 (4-6) (2007) 1048–1073.

[19] F. Tornabene, N. Fantuzzi, E. Viola, R. C. Batra, Stress and strain recovery for functionally graded free-form and doubly-curved sandwich shells using higher-order equivalent single layer theory, Composite Structures 119 (2015) 67–89.

[20] S. Ambartsumian, Two analysis method for two-layer orthotropic shells, Izv An Arm SSR Seiya Fiz-Matem nauk 10 (2) (1957).

[21] H. Murakami, Laminated composite plate theory with improved in-plane responses, Journal of Applied Mechanics 53 (3) (1986) 661–666.

[22] E. Carrera, Multilayered shell theories accounting for layerwise mixed description, part 1: Governing equations, AIAA journal 37 (9) (1999) 1107–1116.

[23] E. Carrera, On the use of the murakami's zig-zag function in the modeling of layered plates and shells, Computers & Structures 82 (7-8) (2004) 541–554.

[24] F. Tornabene, N. Fantuzzi, M. Bacciocchi, E. Viola, Accurate inter-laminar recovery for plates and doubly-curved shells with variable radii of curvature using layer-wise theories, Composite Structures 124 (2015) 368–393.

[25] A. Milazzo, Mixed finite elements for nonlocal elastic multilayered composite plate refined theories, Composite Structures (2020) 112291.

[26] M. D'Ottavio, A sublaminate generalized unified formulation for the analysis of composite structures, Composite Structures 142 (2016) 187–199.

[27] E. Carrera, Theories and finite elements for multilayered, anisotropic, composite plates and shells, Archives of Computational Methods in Engineering 9 (2) (2002) 87–140.

[28] E. Carrera, Theories and finite elements for multilayered plates and shells: a unified compact formulation with numerical assessment and benchmarking, Archives of Computational Methods in Engineering 10 (3) (2003) 215–296.

[29] E. Carrera, M. Cinefra, M. Petrolo, E. Zappino, Finite element analysis of structures through unified formulation, John Wiley & Sons, 2014.

[30] L. Vu-Quoc, X. Tan, Optimal solid shells for non-linear analyses of multilayer composites. i. statics, Computer methods in applied mechanics and engineering 192 (9-10) (2003) 975–1016.

[31] E. Carrera, A. Pagani, S. Valvano, Shell elements with through-the-thickness variable kinematics for the analysis of laminated composite and sandwich structures, Composites Part B: Engineering 111 (2017) 294–314.

[32] G. Li, E. Carrera, Shell finite element models with local kinematic refinements based on reissner's mixed variational theorem with layer-wise descriptions, Composite Structures 250 (2020) 112587.

[33] G. Payette, J. Reddy, A seven-parameter spectral/hp finite element formulation for isotropic, laminated composite and functionally graded shell structures, Computer methods in applied mechanics and engineering 278 (2014) 664–704.

[34] M. G. Rivera, J. Reddy, M. Amabili, A new twelve-parameter spectral/hp shell finite element for large deformation analysis of composite shells, Composite Structures 151 (2016) 183–196.

[35] D. Versino, M. Gherlone, M. Di Sciuva, Four-node shell element for doubly curved multilayered composites based on the refined zigzag theory, Composite Structures 118 (2014) 392–402.

[36] D. Versino, H. M. Mourad, T. O. Williams, A global–local discontinuous galerkin shell finite element for small-deformation analysis of multi-layered composites, Computer Methods in Applied Mechanics and Engineering 271 (2014) 269–295.

[37] D. Versino, H. M. Mourad, T. O. Williams, F. L. Addessio, A global–local discontinuous galerkin finite element for finite-deformation analysis of multilayered shells, Computer Methods in Applied Mechanics and Engineering 283 (2015) 1401–1424.

[38] B. Wu, A. Pagani, W. Chen, E. Carrera, Geometrically nonlinear refined shell theories by carrera unified formulation, Mechanics of Advanced Materials and Structures (2019) 1–21.

[39] H. Mallek, H. Jrad, M. Wali, F. Dammak, Geometrically nonlinear finite element simulation of smart laminated shells using a modified first-order shear deformation theory, Journal of Intelligent Material Systems and Structures 30 (4) (2019) 517–535.

[40] M. F. Caliri Jr, A. J. Ferreira, V. Tita, A review on plate and shell theories for laminated and sandwich structures highlighting the finite element method, Composite Structures 156 (2016) 63–77.

[41] C.-P. Wu, C.-Y. Lee, Differential quadrature solution for the free vibration analysis of laminated conical shells with variable stiffness, International Journal of Mechanical Sciences 43 (8) (2001) 1853–1869.

[42] F. Tornabene, N. Fantuzzi, M. Bacciocchi, The local gdq method applied to general higher-order theories of doubly-curved laminated composite shells and panels: the free vibration analysis, Composite Structures 116 (2014) 637–660.

[43] F. Tornabene, S. Brischetto, 3d capability of refined gdq models for the bending analysis of composite and sandwich plates, spherical and doubly-curved shells, Thin-Walled Structures 129 (2018) 94–124.

[44] A. Ferreira, E. Carrera, M. Cinefra, C. Roque, Analysis of laminated doubly-curved shells by a layerwise theory and radial basis functions collocation, accounting for through-the-thickness deformations, Computational Mechanics 48 (1) (2011) 13–25.

[45] S. Bahrami, F. Shirmohammadi, M. M. Saadatpour, Vibration analysis of thin shallow shells using spectral element method, Applied Mathematical Modelling 44 (2017) 470–480.

[46] W. H. Reed, T. Hill, Triangular mesh methods for the neutron transport equation, Tech. rep., Los Alamos Scientific Lab., N. Mex.(USA) (1973).

[47] D. N. Arnold, F. Brezzi, Cockburn, B., L. D. Marini, Unified analysis of discontinuous galerkin methods for elliptic problems, SIAM journal on numerical analysis 39 (5) (2002) 1749–1779.

[48] G. N. Wells, N. T. Dung, A c0 discontinuous galerkin formulation for kirchhoff plates, Computer Methods in Applied Mechanics and Engineering 196 (35-36) (2007) 3370–3380.

[49] L. Noels, R. Radovitzky, A new discontinuous galerkin method for kirchhoff–love shells, Computer Methods in Applied Mechanics and Engineering 197 (33-40) (2008) 2901–2929.

[50] P. Hansbo, M. G. Larson, A posteriori error estimates for continuous/discontinuous galerkin approximations of the kirchhoff–love plate, Computer methods in applied mechanics and engineering 200 (47-48) (2011) 3289–3295.

[51] A. Bonito, R. H. Nochetto, D. Ntogkas, Discontinuous galerkin approach to large bending deformation of a bilayer plate with isometry constraint, Journal of Computational Physics 423 (2020) 109785. doi:https://doi.org/10.1016/j.jcp.2020.109785.

[52] D. N. Arnold, F. Brezzi, L. D. Marini, A family of discontinuous galerkin finite elements for the reissner–mindlin plate, Journal of Scientific Computing 22 (1-3) (2005) 25–45.

[53] P. R. Bösing, A. L. Madureira, I. Mozolevski, A new interior penalty discontinuous galerkin method for the reissner–mindlin model, Mathematical Models and Methods in Applied Sciences 20 (08) (2010) 1343–1361.

[54] B. L. Talamini, R. Radovitzky, A discontinuous galerkin method for nonlinear shear-flexible shells, Computer methods in applied mechanics and engineering 303 (2016) 128–162.

[55] V. Gulizzi, I. Benedetti, A. Milazzo, An implicit mesh discontinuous galerkin formulation for higher-order plate theories, Mechanics of Advanced Materials and Structures 27 (17) (2020) 1494–1508.

[56] V. Gulizzi, I. Benedetti, A. Milazzo, A high-resolution layer-wise discontinuous galerkin formulation for multilayered composite plates, Composite Structures (2020) 112137.

[57] I. Benedetti, V. Gulizzi, A. Milazzo, Layer-wise discontinuous galerkin methods for piezoelectric laminates, Modelling 1 (2) (2020) 198–214.

[58] X. Du, G. Zhao, W. Wang, Nitsche method for isogeometric analysis of reissner–mindlin plate with non-conforming multi-patches, Computer Aided Geometric Design 35 (2015) 121–136.

[59] V. Oliveri, A. Milazzo, A rayleigh-ritz approach for postbuckling analysis of variable angle tow composite stiffened panels, Computers & Structures 196 (2018) 263–276.

[60] V. Oliveri, A. Milazzo, P. M. Weaver, Thermo-mechanical post-buckling analysis of variable angle tow composite plate assemblies, Composite Structures 183 (2018) 620–635.

[61] V. Gulizzi, V. Oliveri, A. Milazzo, Buckling and post-buckling analysis of cracked stiffened panels via an x-ritz method, Aerospace Science and Technology 86 (2019) 268–282.

[62] P. G. Ciarlet, An introduction to differential geometry with applications to elasticity, Journal of Elasticity 78 (1-3) (2005) 1–215.

[63] T. Ting, Anisotropic Elasticity: Theory and Applications, Oxford Engineering Science Series, Oxford University Press, 1996.
URL https://books.google.it/books?id=RxBoH9GyPkEC

[64] M. Smith, ABAQUS 6.14 Documentation, Dassault Systèmes, 2014, providence, RI, USA.

[65] A. Ruban, J. Gajjar, Fluid Dynamics: Classical fluid dynamics, Fluid Dynamics, Oxford University Press, 2014.